

1
2
3
4
5
6
7
8
9
10
11
12
13
14
15
16
17
18
19
20
21
22
23
24
25
26
27
28
29
30
31
32

A large field of view two-photon mesoscope with subcellular resolution for *in vivo* imaging

Sofroniew, N. J.^{1,*}, Flickinger, D.^{1,*}, King, J.², Svoboda, K.¹

¹ Janelia Research Campus, Ashburn VA 20147, USA

² Vidrio Technologies, Ashburn VA 20147, USA

* These authors contributed equally to this work

Abstract

Imaging is used to map activity across populations of neurons. Microscopes with cellular resolution have small (< 1 millimeter) fields of view and cannot simultaneously image activity distributed across multiple brain areas. Typical large field of view microscopes do not resolve single cells, especially in the axial dimension. We developed a 2-photon random access mesoscope (2p-RAM) that allows high-resolution imaging anywhere within a volume spanning multiple brain areas (Ø 5 mm x 1 mm cylinder). 2p-RAM resolution is near diffraction limited (lateral, 0.66 µm, axial 4.09 µm at the center; excitation wavelength = 970 nm; numerical aperture = 0.6) over a large range of excitation wavelengths. A fast three-dimensional scanning system allows efficient sampling of neural activity in arbitrary regions of interest across the entire imaging volume. We illustrate the use of the 2p-RAM by imaging neural activity in multiple, non-contiguous brain areas in transgenic mice expressing protein calcium sensors.

33 **Introduction**

34

35 Over the last ten years cellular calcium imaging has become widely used to image
36 activity in neuronal populations (Grienberger and Konnerth 2012, Peron et al. 2015a).
37 Calcium imaging samples activity of all labeled neurons in an imaging volume and can
38 readily be combined with visualization of cell type markers to analyze activity in specific
39 cell types, the nodes of neural circuits (Kerlin et al. 2010, Fu et al. 2014, Peron et al.
40 2015a).

41

42 The development of sensitive protein sensors for neuronal function has been a major
43 driver for cellular activity imaging *in vivo* (Nagai et al. 2004, Tian et al. 2009, Horikawa
44 et al. 2010, Zhao et al. 2011, Chen et al. 2013, Dana et al. 2016). More sensitive
45 indicators allow measurement from larger numbers of neurons at fixed signal-to-noise
46 ratios (SNR) (Wilt et al. 2013, Peron et al. 2015a). Future improvements in protein
47 sensors are expected to further increase the numbers of neurons that can be probed
48 simultaneously.

49

50 The vast majority of cellular imaging *in vivo* has been done with 2-photon microscopy
51 (Denk and Svoboda 1997). 2-photon microscopy confines excitation in scattering tissue,
52 which in turn underlies three-dimensional contrast with subcellular resolution (Denk et al.
53 1994). 2-photon microscopy demands that individual resolution elements (on the order of
54 $1 \mu\text{m}^3$) are sampled sequentially, limiting its speed. Spurred by the development of fast
55 solid state cameras, wide-field methods such as wide-field microscopy (Ziv et al. 2013),
56 light-field microscopy (Prevedel et al. 2014), and light-sheet microscopy (Holekamp et
57 al. 2008, Ahrens et al. 2013) have been used to measure neural activity. Scattering and
58 out-of-focus fluorescence rapidly degrade signal and contrast when imaging in scattering
59 tissue with wide-field methods compared to 2-photon microscopy (Peron et al. 2015a).
60 As a consequence, at any point in the image, signals from multiple neurons are mixed
61 together. Unmixing these signals to extract neural activity of individual neurons is a
62 challenging computational problem, which remains unsolved in general. In contrast, the
63 high resolution and image contrast provided by 2-photon microscopy allows extraction of
64 fluorescence signals corresponding to the activity of individual neurons and subcellular
65 compartments (Stosiek et al. 2003, Sato et al. 2007, Akerboom et al. 2012, Chen et al.
66 2013) (Petreanu et al. 2012).

67

68 Together with calcium imaging, 2-photon microscopy is now routinely used to examine
69 behavior-related activity in populations of neurons (Harvey et al. 2012, Huber et al. 2012,
70 Peron et al. 2015b). The majority of studies image only dozens to hundreds of neurons in
71 one brain region at a time. The advent of sensitive protein indicators for calcium (Nagai
72 et al. 2004, Tian et al. 2009, Horikawa et al. 2010, Zhao et al. 2011, Chen et al. 2013) and
73 transgenic animals expressing these indicators (Dana et al. 2014, Madisen and al 2015)
74 promises much higher throughput. 2-photon microscopy has already been used together
75 with GCaMP6 (Chen et al. 2013) to measure activity in approximately 1800 pyramidal
76 neurons at 7 Hz using 50 mW of power at the sample (Peron et al. 2015b). Optimization
77 of the delivered laser power and 2-photon excitation efficiency will allow tracking of

78 more than 10,000 pyramidal neurons at similar signal-to-noise ratios and sampling
79 frequencies. This opens up the possibility of tracking representative neuronal populations
80 across multiple brain regions.

81

82 Even relatively simple animal behaviors involve multiple brain regions, which are often
83 non-contiguous (Hernandez et al. 2010, Guo et al. 2014). Simultaneous tracking of
84 activity in these brain areas is not possible using standard microscopes, because
85 mechanical movement of microscopes or specimens is slow. High-resolution microscopes
86 have fields of view (FOV) that are smaller than most brain areas, whereas large FOV
87 microscopes have small numerical apertures and cannot resolve individual neurons. To
88 bridge the gap between single cells and brain regions we developed a mesoscale 2-photon
89 microscope capable of imaging a FOV of 5 mm, with subcellular resolution. We use the
90 term ‘mesoscale microscopy’ to refer to imaging with subcellular resolution and fields of
91 view spanning multiple brain areas (several millimeters).

92

93 We implemented fast lateral and axial scanning to both maximize the number of neurons
94 that can be sampled nearly simultaneously and the flexibility in choosing the imaged
95 neurons. The fluorescence signal collected per unit time is ultimately limited by the
96 average power that can be delivered to the specimen, which in turn is limited by heating.
97 In the mouse brain the maximum allowed power is approximately $P_{\max} = 200$ mW
98 (unpublished observations). The signal rate for one scanning beam is $S_l = a P_{\max}^2$, where
99 a is a parameter that depends on the illumination, the experimental preparation (e.g. the
100 type and concentration of the fluorescent probe), and fluorescence detection. In another
101 popular scheme the excitation beam is partitioned into n beams for multiplexed excitation
102 (Lecoq et al. 2014, Stirman et al. 2015). Dividing the power into n laser foci for
103 multiplexed imaging, the signal is $S_n = a n (P_{\max}/n)^2$. This division corresponds to
104 reduced overall signal levels (by $1/n$) and a corresponding reduction in the number of
105 neurons sampled, at fixed signal-to-noise ratio. Increasing the power of each individual
106 beam beyond a total (summed) power of $P_{\max} = 200$ mW would cause heating and
107 associated damage. Given the relatively slow dynamics of calcium-related fluorescence
108 (Peron et al. 2015b), serial scanning with a single laser focus maximizes the number of
109 neurons that can be probed.

110

111 Several 2-photon microscopes have been designed for large field of view *in vivo* imaging.
112 Tsai *et al* designed an elegant scanning system based on off-the-shelf components,
113 producing a scan field of 10 mm (Tsai et al. 2015). Stirman *et al* used a custom objective
114 (Stirman et al. 2014) with a field of view of 3.5 mm. Neither system provides subcellular
115 resolution in the axial dimension (14 μm and 12 μm , respectively), implying that signals
116 from multiple neurons and neuropil may be conflated. In current implementations these
117 instruments use standard galvo mirrors, which are too slow for some types of functional
118 imaging. These microscopes also do not implement rapid axial scanning, which is critical
119 for targeting specific neurons in different parts of the FOV. In addition, the microscopes
120 are corrected for aberrations at only one excitation wavelength (800 nm and 910 nm
121 respectively), limiting their use to a subset of fluorescent probes. A large FOV (5 mm)
122 mesolens for confocal microscopy, with numerical aperture 0.47, has also been reported
123 (McConnell et al. 2016).

124

125 We have developed a 2-photon random access mesoscope (2p-RAM), optimized for
126 imaging populations of neurons in multiple brain regions during behavior. 2p-RAM
127 provides diffraction-limited resolution in a cylindrical volume (\varnothing 5 mm x 1 mm). It is
128 fully corrected for excitation light in the 900-1070 nm range, allowing 2-photon imaging
129 of most widely used fluorescent proteins. 2p-RAM is based on a fast three-dimensional
130 scanning system that allows random access to hundreds of thousands of neurons for
131 targeted interrogation.

132

133 **Results**

134

135 We developed a 2-photon random access mesoscope (2p-RAM) with subcellular
136 resolution. We first outline the key specifications, which correspond to specific
137 engineering challenges. We then explain the optical path of the mesoscope, followed by a
138 brief description of the design process. Finally we illustrate the mesoscope performance
139 in calibration experiments and imaging neural activity *in vivo*.

140

141 **Key specifications**

142

143 First, the diameter of the FOV should be five millimeters. This size allows sampling of
144 most cortical regions in the mouse brain that are nearly coplanar. For example, it would
145 be possible to image the primary somatosensory cortex, the primary motor cortex and
146 parts of secondary motor cortex nearly simultaneously (Figure 1A). Second, the
147 mesoscope should have better than cellular resolution, implying axial resolutions
148 substantially smaller than the typical size of a soma (diameter, 10 μ m) (Peters and
149 Kaiserman-Abramof 1970). We specified a numerical aperture (NA) of 0.6, which
150 translates to approximately 0.61 μ m lateral resolution and 4.25 μ m axial resolution (for λ
151 = 970 nm; Figure 1B) (Zipfel et al. 2003). Third, the mesoscope should produce
152 diffraction-limited performance and high two-photon excitation efficiency over the range
153 of λ = 900 – 1070 nm. This spectral range corresponds to fluorescent protein sensors
154 based on GFP and various red fluorescence proteins (Akerboom et al. 2013). Fourth, the
155 mesoscope should maximize the collection of fluorescence signal, ideally with a large
156 collection NA. We specified a collection NA of 1.0 (specifications listed Figure 1C).

157

158 Fifth, a key challenge for mesoscale 2-photon microscopy is efficient laser scanning.
159 Faster scanning provides better time resolution for measurements of neural activity,
160 reduced photodamage, and tracking larger numbers of neurons. Rapid scanning methods
161 rely on resonant scanning mirrors (Fan et al. 1999) or acousto optic deflectors (AODs)
162 (Reddy and Saggau 2005), both of which have scan angles on the order of a few degrees,
163 corresponding to relatively small (several hundred μ m) scans in the specimen plane. To
164 access the entire scan field rapidly we designed a lateral scan unit with multiple scanners
165 in series. A fast resonant scan is moved over the specimen in a flexible manner using a
166 galvanometer scanner, allowing rapid sampling of activity in widely dispersed brain
167 regions (Figure 1D).

168

169 The sixth and final challenge is scanning along the optical axis of the microscope. In

170 most scanning microscopes, focusing is achieved by moving the objective. Because of the
171 mechanical inertia of the bulky objective, focusing is more than two orders of magnitude
172 slower than lateral scanning (Gobel et al. 2007). This limit is unacceptable for mesoscale
173 imaging because the structures of interest to be sampled in different brain regions are
174 typically in focal planes that differ by up to several hundred micrometers (Figure 1E). We
175 addressed this problem by implementing a rapid remote focusing unit in which a light-
176 weight mirror is moved instead of the objective (Botcherby et al. 2012). Rapid remote
177 focusing also allowed us to relax flatness of field specifications, because rapid focusing
178 can partially correct for curved scan fields online.

179

180 **Implementation**

181

182 *Overview*

183

184 The 2p-RAM was assembled on a vertically mounted breadboard (Figure 2A, 2C, 2E).
185 The refractive optics of the microscope are predicted to introduce 25,000 fs² group-delay
186 dispersion (GDD) (at $\lambda=1000$ nm). GDD will cause the light arriving at the focus to be
187 spread out in time, resulting in reduced efficiency for two-photon excitation (Denk et al.
188 1995). To reduce GDD at the sample, the Ti:Sapphire laser beam first passed through a
189 prism-based GDD compensation unit (Akturk et al. 2006) (Figure 2B). With GDD
190 compensation enabled, we measured a pulse width of 106 fs at the sample using an
191 autocorrelator (Carpe; APE) (see Figure 2 Supplement 2), comparable to the pulse width
192 emitted by our laser (Mai Tai HP; Spectra Physics).

193

194 The microscope is motorized to allow flexible access to the specimen: it moves in x, y
195 (> 50 mm travel); it rotates around an axis that passes through the specimen plane and is
196 parallel to the long axis of the microscope (± 20 degrees travel); it moves up and down
197 along the beam axis for coarse focusing (travel +38 mm -13 mm). Since the microscope
198 moves with respect to the laser, the beam was threaded into the microscope through a
199 multi-stage periscope.

200

201 *Remote focus unit*

202

203 Within the core of the microscope, the beam first enters the remote focus (RF) unit
204 through a polarizing beam splitting cube and a quarter wave plate. The RF unit consists
205 of a custom RF objective, and a small mirror (mass, 170 mg; PF03-03-P01, Thorlabs)
206 mounted on a voice coil (LFA 2010 with a sca814 controller; Equipment Solutions). The
207 beam passes through the RF objective and is reflected by the mirror back through the RF
208 objective. The quarter wave plate and polarizing beam splitting cube together then direct
209 the beam into the lateral scan unit. The coatings of the RF objective were optimized for
210 high transmission in the IR range. These coatings and the small number of elements (5)
211 combined to give high transmission through the RF objective (97%).

212

213 The entrance aperture of the RF objective is conjugated to the entrance aperture of the
214 imaging objective. The RF mirror is approximately conjugate to the focus in the
215 specimen plane. Axial movement of the RF mirror changes the axial location of the focus

216 in the specimen (scale factor, 1.23; i.e. a 100 μm move of the RF mirror causes a 123 μm
217 move of the focus). Depending on the axial position of the RF mirror, the wavefront
218 entering the imaging objective will be converging, parallel, or diverging. For standard
219 microscope objectives, which obey the sine condition, only parallel rays will converge to
220 a diffraction-limited point in the specimen (Born and Wolf 1980). Spherical wavefronts
221 in the objective pupil will produce spherical aberration at the focus. Rays entering the
222 objective back aperture at its periphery will focus to a different point along the axis,
223 thereby producing a larger focal volume with lower peak intensity. These spherical
224 aberrations degrade resolution and contrast. The RF objective was designed to counteract
225 the spherical aberrations produced by the imaging objective, so that diffraction-limited
226 imaging can be achieved throughout the microscope's imaging volume (Botcherby et al.
227 2012). The imaging objective also has axial chromatic aberration that varies with RF
228 depth, which is compensated by the RF objective. The RF unit allows rapid axial
229 movement of the focal plane, since the RF mirror can be moved much faster than the
230 objective or the specimen.

231

232 *Scanning system*

233

234 We designed a lateral scanning unit to efficiently scan arbitrary regions of interest in the
235 FOV of the microscope. A resonant scanner produces a fast line scan (24 kHz line rate)
236 (CRS 12K, Cambridge Technology). Because of the limited angular range of the scanner
237 (10 degrees, optical peak-to-peak) this results in a scan range of 0.6 mm or less in the
238 specimen plane. This scan line is moved over the specimen using a pair of galvo
239 scanners.

240

241 Microscopes using remote focusing have to deal with non-planar wavefronts in their
242 pupil locations. Maintaining conjugation between all scan mirrors and optic pupils is a
243 critical issue for these microscopes. Otherwise, the movement of any scan mirror that is
244 not conjugated to a subsequent optic pupil, such as the entrance pupil of the objective,
245 will cause a lateral shift of the wavefront at that pupil. Wavefront non-planarity and
246 lateral shift can cause significant optical aberrations.

247

248 The beam is directed through a pupil relay (PR1; magnification, 0.44) into the resonant
249 scanner (open aperture, 4.8 mm), and then through a second identical pupil relay in
250 reverse (PR2; magnification, 2.3) into a virtually conjugated galvo pair (VCGP). The
251 VCGP unit conjugates the x and y scan galvo pair without a large-aperture relay made
252 from refractive optics. Alternatively conjugation could have been accomplished using a
253 custom pupil relay using refractive optics. However, due to its large size, this relay would
254 be the most complex and expensive part of the microscope. The VCGP provides a
255 compact and cost-effective solution.

256

257 The VCGP uses three galvo mirrors (rather than two) to ensure that the pupils of the x
258 and y scanning galvos are coincident. The first two mirrors (open aperture, 20 mm;
259 Cambridge Technology 6M2420X40B025S4 mirror on 6240HM40B galvo) are moved in
260 the same plane so that the beam rotates about a pupil centered on the third mirror (open
261 aperture, 14 mm, Cambridge 6M2314X44B025S4 mirror on 6231HM44C galvo), which

262 rotates in the orthogonal direction. In this manner the pupil remains substantially
263 stationary over a large scan range. The 20 mm, virtually conjugated galvo mirrors each
264 have a scan range of 40 deg (optical peak-to-peak, OPTP). However, the virtual
265 conjugate arrangement of these mirrors results in a total scan range of 32.2 deg OPTP at
266 the following pupil. The 14 mm galvo mirror has a scan range of 44 deg OPTP. The
267 20 mm mirrors can perform a step across their entire range with step-and-settle time of
268 3.4 ms. Smaller steps with these mirrors, and all steps with the 14 mm mirror, are faster.

269

270 *Objective*

271

272 The exit pupil of the VCGP is imaged by another pupil relay (PR3; magnification, 2.3)
273 onto the entrance pupil (diameter, 25.6 mm) of the imaging objective (NA, 0.6, focal
274 length 21 mm) (Figure 2D). The excitation beam is routed into the imaging objective
275 using a shortpass dichroic (DM1; size 70 x 99 mm; 750 nm shortpass custom coating
276 design from Alluxa). The front lens has a tip diameter of 15 mm. The distance between
277 the edge of the front lens and the top of the specimen is 2.7 mm. Because remote
278 focusing moves the focal plane into the specimen without movement of the objective or
279 specimen, the effective working distance of the objective is larger than 3 mm. *In vivo*
280 imaging is usually performed through a microscope coverglass (Trachtenberg et al. 2002,
281 Holtmaat et al. 2009). The optical system is corrected to operate in a diffraction-limited
282 manner through a # 4 coverglass (450 μm of BK7 glass; equivalent to a stack of three # 1
283 coverglasses). Power transmission through the entire system is 13% (Figure 2B).

284

285 *Fluorescence collection path*

286

287 Fluorescence light passes through the primary dichroic (DM1) into the detector arm of
288 the microscope. An optional second dichroic mirror (DM2) allows for an ancillary optical
289 path for one-photon imaging and photostimulation. A third dichroic mirror (DM3)
290 divides the fluorescence path into two signals, each directed into one of two GaAsP
291 photomultiplier tubes (PMTs) (Hamamatsu H11706-40).

292

293 In a 2-photon microscope, the etendue of fluorescence light collection by the objective
294 lens must be matched or exceeded by the etendue of the light detector. This condition is
295 critical for optimal detection of precious signal photons. For most microscopes this
296 condition is not an issue, as PMTs have photocathodes that are much larger than the
297 objective FOV, as well as sizable collection angles (Tsai et al. 2002). For the 2p-RAM
298 the imaging objective collects emitted light with an NA of 1.0, and a collection FOV of 6
299 mm (Oheim et al. 2001). The diameter of the imaging objective pupil relevant for
300 fluorescence detection is 42 mm. The etendue of this collected emission light exceeds the
301 etendue of the current state-of-the-art PMTs which have a photocathode diameter of 5
302 mm and a usable NA of approximately 0.9 (unpublished measurements). This makes it
303 impossible for all of the fluorescence light collected by the objective to be directed onto
304 the PMT using conventional imaging schemes (Mainen et al. 1999, Tsai et al. 2002). To
305 overcome this problem we used oil to directly couple a custom-made condenser lens to
306 the glass enveloping the PMT. This allowed the collection NA of the PMT to reach 1.4.
307 In this manner all of the fluorescence that is collected by the imaging objective is

308 projected onto the PMT for detection (not counting reflection losses).

309

310 Our collection path does not image the back pupil of the objective onto the PMT (Denk et
311 al. 1995, Mainen et al. 1999), as that design would require significantly more complex
312 collection optics. As a result, the spatial distribution of the signal on the PMT
313 photocathode varies with location of the signal source within the sample. The spot size of
314 the projected light from a point source in the sample on the photocathode varies from 1.5
315 mm to 2.7 mm, depending on the location of the source point. The microscope image is
316 therefore sensitive to inhomogeneities in the photosensitivity of the PMT photocathode.
317 For the most critical applications it may be necessary to select PMTs with homogeneous
318 photocathodes or employ computational methods to correct for the inhomogeneity.

319

320 **Optical design**

321

322 The excitation path, including the RF objective, pupil relays 1-3, and imaging objective,
323 was modeled in silico (Zemax). We searched for configurations of optical elements with
324 diffraction-limited performance and high two-photon excitation efficiency across the
325 $\varnothing 5 \times 1$ mm imaging volume, for excitation wavelengths over the range 900-1070 nm.
326 Performance was assessed using the Strehl ratio (SR), which is a measure of the quality
327 of optical image formation. Without aberrations an optical system has $SR = 1$; aberrations
328 drive SR toward zero. We optimized for $SR > 0.8$ across the imaging volume, a
329 commonly used criterion for diffraction-limited performance.

330

331 Two-photon excitation efficiency depends on the propagation time delay difference
332 (PTD) for different rays across the pupil of the system (Estrada-Silva et al. 2009). For
333 PTD not much less than the pulse duration, the efficiency of two-photon excitation would
334 be severely reduced. PTD was kept to less than 50 fs (rms). As far as we know no other
335 microscopy system has been designed with optimization of the PTD as a design criterion.

336

337 Other design parameters included: The number, size and complexity of the optical
338 elements; focusing range of the RF unit; nature and cost of the optical glasses. Field
339 curvature was limited to less than 160 μm over the 5 mm FOV. Finally, tolerancing was
340 performed to minimize sensitivities and guide manufacturing (Code V). No stock lenses
341 were used for these modules, as doing so in most cases would not allow sufficient control
342 over the tolerances to meet performance specifications. The element count for each
343 module was: RF objective, 5; pupil relay 1/2 (identical), 4; pupil relay 3, 6; imaging
344 objective, 6. (The modules were manufactured by Jenoptik. Jupiter, FI; part numbers RF
345 objective: 14163200, pupil relay 1/2: 14506000, pupil relay 3: 14163100, imaging
346 objective: 14163000; for a table of critical distances between these elements necessary
347 for assembly see Figure 2 Supplement 1). A detailed description of the custom optics and
348 the design process will be published elsewhere.

349

350 **Calibration experiments**

351

352 *Brightness across the field of view*

353

354 We measured the signal brightness across the FOV. In a homogeneous sample, such as a
355 solution of fluorophore, image brightness is determined by the two-photon excitation
356 efficiency and the collection efficiency for fluorescence, both of which depend on
357 position in the FOV. We acquired an image of a 1 mm thick bath of fluorescein ($\lambda = 970$
358 nm). At an imaging depth of 500 μm , brightness was constant up to approximately
359 2.5 millimeters from the center, beyond which image brightness collapsed (Figure 3). The
360 image showed inhomogeneities across the resonant scan (608 μm), apparent as shading in
361 the vertical stripes in Figure 3A. The shading is produced by wave front error introduced
362 by pupil relay 2 during rapid resonant scanning. Smaller resonant scans would reduce this
363 shading. Inhomogeneities in brightness within the specified FOV were on the order of
364 30 % (Figure 3C), including a small dip in brightness in the center of the field (this dip is
365 caused by spatial inhomogeneity in the PMT sensitivity across its photocathode; see
366 below).

367

368 *Resolution*

369

370 We next measured the resolution of the microscope. Fluorescent microbeads (0.5 μm ;
371 Fluoresbrite Calibration Grade YG microspheres CAT# 18859, Polysciences Inc.) were
372 embedded in agar (1.5 %; Agarose, Type III-A Sigma A9793) at a dilution of 1:10,000.
373 Three-dimensional images stacks containing images of beads were collected at various
374 positions in the imaging volume ($\lambda = 970$ nm). Resolution was estimated based on the
375 lateral and axial full-width-at-half-max (FWHM) of the bead images (Figure 4). The
376 lateral FWHM of the bead image was 0.66 ± 0.003 μm (SEM) and the axial FWHM was
377 4.09 ± 0.06 μm (SEM). Approximately 2 millimeters from the center of the FOV, the
378 resolution started to degrade gradually (Figure 4I, J, K). At the edge of the FOV (2.5 mm
379 from the center) the lateral FWHM was 0.89 ± 0.006 μm (SEM), and the axial FWHM
380 6.88 ± 0.07 μm (SEM). At the center of the FOV, performance was diffraction-limited up
381 to 1 mm deep into the sample (Figure 4 Supplement 1). This performance was similar at
382 different positions in the field and different imaging depths up to 1 mm into the sample
383 (Figure 4 Supplement 2). Resolution was consistent across wavelengths from 900 nm to
384 1040 nm (the limit of the tuning range of our Ti:Sapphire laser) (Figure 4 Supplement 3).
385 Resolution also remained essentially unchanged for small (up to $\pm 2.5^\circ$) tilts of the
386 coverglass with respect to the beam axis (Figure 4 Supplement 4). We conclude that the
387 2p-RAM is capable of subcellular resolution over the entire imaging volume ($\varnothing 5 \times 1$ mm
388 cylinder) and is robust to moderate misalignments.

389

390 The brightness of the imaged beads dropped off towards the edge of the FOV (up to a
391 factor of four 2.5 mm from the center of the FOV; Figure 4K). This is consistent with the
392 observed increase in the size of the PSF (Figure 4J). In 2-photon microscopy, the
393 brightness of objects that are on the order of, or smaller than the diffraction limit are
394 highly sensitive to degradation in the PSF. Decreased fluorescence collection efficiency
395 at the edges of the FOV could also contribute to dimmer images at the edge of the FOV.
396 Conversely, resolution was consistent across the center of the field, (Figure 4I, J)
397 suggesting that the dip in brightness (Figure 3) at the center of the field is likely due to a
398 dip in PMT sensitivity in the center of the FOV (see below).

399

400 *Collection efficiency*

401

402 Biological 2-photon microscopy is typically limited by photodamage produced by
403 excitation light. Better detection of fluorescence signal allows reduced excitation for
404 fixed SNR. Optimizing fluorescence detection is therefore a critical aspect of designing a
405 2-photon microscope for *in vivo* imaging. In scattering samples the objective numerical
406 aperture and its FOV contribute to fluorescence detection (Oheim et al. 2001). We
407 therefore characterized the signal collection efficiency of our system as a function of
408 position of the signal source and numerical aperture (Figure 5).

409

410 We separately varied the position of a light source and its NA while measuring the signal
411 detected by the PMT (Figure 5A). A pinhole was mounted in front of the light source
412 (LED) and imaged using an imaging system into the specimen plane. The NA of the light
413 cone was controlled using an aperture in an intervening aperture plane. The microscope
414 was moved on a 0.5 millimeter grid around this assembly.

415

416 The PMT signal was remarkably constant across the FOV and beyond (Figure 5B). The
417 signal showed a modest dip in the center of the FOV (approximately 20% reduced
418 sensitivity). This dip was tracked down to inhomogeneous sensitivity on the PMT
419 photocathode (data not shown). This dip also likely accounts for the lower brightness at
420 the center of the field (Figure 3).

421

422 We next changed the NA of the light source. The total light entering the objective was
423 roughly proportional to the second power of the NA (Figure 5C). The signal detected by
424 the PMT was proportional to the signal entering the objective up to NA 1.0, the specified
425 NA for fluorescence detection of the IO (Figure 5C, 5D). We conclude that our
426 fluorescence collection system performs nearly optimally across the specified FOV
427 (\varnothing 5 mm). The overall transmission of the collection path, including reflection and
428 transmission losses, was 71 %.

429

430 *Field curvature and its correction using remote focusing*

431

432 To characterize the field curvature of the microscope we imaged a thin and flat
433 fluorescent sample (Figure 6A). If the scan transects the sample the fluorescent image is a
434 circle (Figure 6B). The radius of the circle increases monotonically as the RF is adjusted
435 downward. In this way we mapped the field curvature of the microscope. The focal
436 position changed by up to 158 μ m at 2.5 mm from the center of the FOV.

437

438 We implemented a field curvature correction by the RF unit in our scan control software.
439 Following a 300 μ m step, the RF mirror settles to better than 2.5 μ m in 6.77 ± 0.02 ms
440 (SEM) (Figure 6, Supplement 1). The correction was done on a line-by-line basis, using
441 the average position of the resonant mirror during the line as the position to correct. This
442 scheme corrects the field curvature associated with movements of the slower galvo
443 mirrors (i.e. along the vertical image stripes). Field curvature along the resonant scan
444 could not be corrected in this manner because the RF unit does not have the necessary

445 bandwidth. Not correcting the field curvature along the resonant axis (Figure 6C, bottom)
446 causes striping artifacts present in the images (Figure 7).

447

448 ***In vivo* imaging**

449

450 We next imaged neurons in transgenic mice expressing fluorescent proteins. Mice were
451 prepared with a stainless-steel head plate and a D-shaped cranial window using standard
452 surgical procedures (Peron et al. 2015b). The D-shaped window was 450 μm thick and
453 made from three layers of custom cut coverglass (Potomac Photonics). The window
454 spanned from the lambda suture to 3 mm anterior of Bregma and from the midline 5 mm
455 laterally, allowing optical access to a large fraction of the cortical surface on the left
456 hemisphere.

457

458 Low magnification, high-resolution images ($\lambda = 970 \text{ nm}$) were acquired in anesthetized
459 mice expressing GCaMP6f in a subset of pyramidal neurons (GP5.17 mice) or GCaMP6s
460 in the vast majority of pyramidal neurons (GP4.3) (Dana et al. 2014). Superficial images
461 showed the vascular pattern on the surface of the brain (GP5.17, Figure 7A, B; GP4.3,
462 Figure, 7C, Movie 1). Higher magnification views revealed single neurons and their
463 dendrites (Figure 7B). Resolution and contrast degrade with imaging depth *in vivo*,
464 caused by aberration and scattering (Ji et al. 2012). However, images of neurons appeared
465 as ring-like structures up to 600 μm deep in the tissue (Movie 1), reflecting GCaMP
466 exclusion from the nucleus (Tian et al. 2009) and demonstrating subcellular resolution of
467 the 2p-RAM.

468

469 Deeper imaging, approximately 450 μm below the surface of the brain, revealed the
470 outlines of the layer 4 barrels of the whisker representation area of the somatosensory
471 cortex, and the lower limb and upper limb somatosensory areas (Figure 7E, 7F, 7
472 Supplement 1A; GP4.3). Layer 4 has decreased fluorescence because stellate cells do not
473 express fluorescent proteins in these mice (Dana et al.).

474

475 We next imaged GFP-labeled nuclei of excitatory neuron in *emx1-Cre x Isl1-h2b-GFP*
476 mice (Madisen et al. 2015). We imaged the full FOV in 2 μm z-steps (up to 600 μm
477 deep) and 1.2 x 1.3 μm^2 pixels (Figure 7 Supplement 2A). We automatically detected
478 nuclei in three dimensions using a peak finding algorithm (`peak_local_max`, `scikit-image`)
479 (Figure 7 Supplement 2B). We detected a total of 207,359 nuclei in the volume (Figure 7
480 Supplement 2C). This is a lower bound on the number of neurons accessible for
481 functional imaging in the 2p-RAM.

482

483 In mice expressing YFP in a sparse subset of pyramidal neurons (YFP-H) (Feng et al.
484 2000) we were able to resolve individual spines (Figure 7 Supplement 3).

485

486 We next imaged neural activity in behaving mice running on a treadmill in tactile virtual
487 reality (Sofroniew et al. 2014, Sofroniew et al. 2015). We imaged a 4.4 mm x 4.2 mm
488 FOV at 1.9 Hz in layer 2/3 (Figure 8 supplement 1A, B, Movie 2; GP4.3 mice). A simple
489 correlation analysis revealed over 3000 active neurons (Figure 8 supplement 1C, D).

490

491 The 2p-RAM can link activity at the level of brain regions and single neurons. For
492 example, low magnification movies showed activity across multiple brain regions
493 including somatosensory, parietal, and motor areas (Figure 8A; GP5.17 mice). We
494 correlated the average activity from an area (region 1) in somatosensory cortex with
495 activity in the rest of brain (Vanni and Murphy 2014)(Figure 8B). We then imaged region
496 1 and three additional, widely separated regions (each $600 \times 600 \mu\text{m}^2$) at higher speed (9.6
497 Hz) (Figure 8C, Movie 3). Individual neurons showed fluorescence transients
498 corresponding to trains of action potentials (Chen et al. 2013). We manually segmented
499 individual neurons in each of the regions and computed the change in fluorescence
500 ($\Delta F/F$) over time (Figure 8E). We measured average activity in region 1 by computing
501 the maximum of the $\Delta F/F$ traces across all neurons in that region at each time point. We
502 then correlated this trace against all the $\Delta F/F$ traces of individual neurons (Figure 8D,
503 8F). Some neurons in the different areas showed high correlation with this average trace,
504 whereas others showed uncorrelated activity (Okun et al. 2015). In this manner, the 2p-
505 RAM can be used to relate activity across nearly the entire dorsal cortex with the activity
506 of individual neurons in specific areas during behavior.

507

508 Discussion

509

510 We designed a 2-photon random access mesoscope (2p-RAM) that allows rapid
511 microscopic investigation of neural tissue over large imaging volumes. The 2p-RAM has
512 a numerical aperture of 0.6 and an imaging volume corresponding to a $\varnothing 5 \times 1$ mm
513 cylinder. The imaging volume is approximately 100-fold larger compared to other
514 microscopes with comparable resolution.

515

516 The 2p-RAM is optimized for high-resolution *in vivo* imaging. Lateral scanning is
517 performed using a resonant scanner in series with a xy galvo scanner. Rapid scanning is
518 achieved by moving the fast resonant scan over the FOV using the galvo mirrors. Even
519 faster and more flexible scanning could potentially be achieved using acousto-optic
520 deflectors (Duemani Reddy et al. 2008) instead of resonant scanners.

521

522 Rapid axial scanning is critical for mesoscale functional imaging in the intact brain. This
523 is because neurons of interest will generally be at different imaging depths in different
524 brain regions. It is also often of interest to interrogate the same brain region at different
525 imaging depths. In the 2p-RAM, axial scanning is based on aberration-free focusing
526 using a remote mirror (Botcherby et al. 2012). The mirror is moved in a plane nearly
527 conjugate to the specimen plane to move the focus. Aberrations are corrected by passing
528 the beam through a RF objective that produces complimentary aberrations to the imaging
529 objective. In published optical arrangements, the beam is scanned laterally first, and is
530 then sent into the RF system (Botcherby et al. 2012). This design puts constraints on the
531 RF objective. In our system the beam is passed through the RF system before lateral
532 scanning. This configuration allowed the etendue, and thus size, complexity, and cost, of
533 the RF objective to be much lower than that of the imaging objective. We also optimized
534 the coatings and the element count of the RF objective to minimize power losses that are
535 normally high in remote focusing systems. The optics subsequent to the RF objective
536 could be made such that the remote focusing is invariant to lateral scanning, and thus

537 diffraction-limited focusing can be achieved over a large volume with this arrangement.
538 Alternative axial scanning techniques, such as rapidly moving the objective (Gobel et al.
539 2007), are impractical due to the large size of the 2p-RAM objective. Electrotunable
540 lenses introduce spherical and chromatic aberrations (Grewe et al. 2011).

541
542 The 2p-RAM has relatively large field curvature (Figure 6). Rapid remote focusing can
543 help to compensate for field curvature in real time during scanning. Online correction of
544 field curvature can only be achieved for the movements produced by the slower galvo
545 scanners. The movements of the resonant scanner are too fast to be fully compensated,
546 because RF systems implemented with either galvos (Botcherby et al. 2012), voice coils
547 (Figure 6 Supplement 1), or piezos (unpublished observations) cannot match the resonant
548 scanning bandwidth. Fast resonant scan lines are by necessity tilted, which is more
549 pronounced close to the edge of the FOV. For many *in vivo* applications the residual field
550 curvature is expected to be only a small inconvenience, because neurons of interest in
551 different brain areas are typically in different focal planes.

552
553 The serial scan system allows for both low-magnification imaging across a large area and
554 high-resolution imaging across smaller, but widely separated, areas. Low-magnification
555 imaging can be combined with online analysis to identify brain areas with particular
556 activity patterns of interest. Once these areas are found, high-resolution imaging can
557 interrogate populations of individual neurons within those areas. The low-magnification
558 image can be used to optimally place these smaller imaging regions around the
559 vasculature.

560
561 We performed GDD compensation to maximize peak power delivered for a given
562 average power. Larger peak power then can be used to maintain the same signal to noise
563 ratio during faster scanning with smaller pixel dwell times. Optimal placement of
564 imaging regions and faster scanning combined with smaller jump times between regions
565 will allow for simultaneous tracking of tens of thousands neurons across the cortex at
566 10 Hz.

567
568 Microscopes with yet larger fields of view are possible. However, given fixed NA, larger
569 fields of view correspond to larger objectives. Larger and PMTs will be required to
570 efficiently collect the fluorescence transmitted by these giant objectives.

571
572 There is considerable interest in more natural, unconstrained, and therefore more variable
573 animal behaviors. Relating the underlying neural population activity to behavior will
574 require single-trial analysis, which is limited by the number of neurons that can be
575 recorded in multiple brain regions (Churchland et al. 2007). Mesoscale recording
576 systems, such as 2p-RAM, allow recordings from thousands of neurons across multiple
577 brain areas. These large numbers are critical to achieve single-trial decoding of neural
578 activity patterns during behavior.

579
580
581

582 **Figure Captions**

583

584 **Figure 1. Specifications for the 2p-RAM.**

585 A) Schematic of the dorsal surface of the mouse cortex (from Allen Brain Atlas, Brain
586 Explorer 2). The overlaid circle corresponds to the specified FOV (\varnothing 5 mm). MOp:
587 primary somatomotor, MOs: secondary somatomotor, SSp-ul: primary somatosensory
588 upper limb, SSp-ll: primary somatosensory lower limb, SSp-un: primary somatosensory
589 unassigned, SSp-tr: primary somatosensory trunk, SSp-bfd: primary somatosensory barrel
590 field, PTLp: posterior parietal association, RSP: retrosplenial, VISam: anteromedial
591 visual, VISpm: posteromedial visual, VISp: primary visual.

592 B) Schematic of a neuron (approximate soma diameter, 10 μ m), and a diffraction limited
593 point spread function (PSF) corresponding to NA 0.6 and 970 nm. Subcellular resolution
594 implies that the PSF must be contained within a single neuron.

595 C) Key specifications for the mesoscope.

596 D) Imaging parameters used in the experiments. In all cases a fast resonant scan (time per
597 scan line, 42 μ s; 24 kHz line rate) is made over patches 608 μ m wide. The time per patch
598 is 42 μ s x number of lines. The entire FOV can be covered in nine stripes. A slow (0.7
599 Hz), high-resolution scan with 3500 lines per stripe was used to cover a large portion the
600 FOV (i). A fast (4.3 Hz), low-resolution scan across the entire scan range has up to 500
601 lines per stripe (iv). More typical scans will involve sampling multiple smaller patches at
602 high resolution and frame rates (v). See implementation for discussion of the scanning
603 patterns.

604 E) Schematic showing a typical use-case. The entire imaging volume is a cylinder with a
605 5 mm diameter and 1 mm depth. The fast scan is made over patches in different parts of
606 the volume.

607

608 **Figure 2. 2p-RAM optics and optomechanics.**

609 A) Optical layout. Several routing mirrors were omitted for clarity. See text for detailed
610 description.

611 B) Power transmission measurements at 970 nm.

612 C) CAD model of the microscope. The microscope was assembled on a vertically
613 mounted breadboard measuring 1.0 m x 0.5 m. The objective is 63 mm wide, 120 mm
614 long, and weighs 1.43 kg.

615 D) Photograph of microscope objective. (D, E, photocredit; Matt Staley).

616 E) Photograph of vertically mounted breadboard.

617

618 **Figure 2. Supplement 1. Distances between the critical 2p-RAM components.**

619 A) CAD model of the microscope with critical distances for assembling the 2p-RAM.
620 PR: pupil relay, RFO: remote focus objective, IO: immersion objective, res.: resonant
621 scan mirror.

622

623 **Figure 2. Supplement 2. Pulse width measurements.**

624 We measured the pulse width (full-width-at-half-max) using an autocorrelator. The
625 autocorrelator was placed after the first telescope and EOM. For a Gaussian laser pulse,
626 the width of the autocorrelation is 1.41 times the pulse width of the individual laser pulse.

627 A) Autocorrelation at the autocorrelator without GDD compensation. B) Autocorrelation

628 at the autocorrelator with GDD compensation. The pulse is now very broad due to the
629 pre-chirp. C) The autocorrelation at the specimen. As a sample we used a uniform
630 fluorescent solution (Sigma F6377, 100 μ M, 1 mm thick) and recorded fluorescence
631 using the PMT.

632

633 **Figure 3. Image brightness.**

634 A) Image of a uniform fluorescent sample (fluorescein solution, Sigma F6377, 100 μ M, 1
635 mm thick under 450 μ m of coverglass, average of 30 frames). The image was acquired in
636 9 stripes, each approximately 600 μ m wide (see Figure 1D, iv for details). The intensity
637 variations in the image are caused by changes both in excitation and collection efficiency
638 across the field.

639 B) Y profile (along slow scan axis) through slice at the central RF position normalized to
640 the peak signal, which was located off the main two axes.

641 C) X profile (along fast scan axis) profile through central slice. The dips in signal at the
642 edge of the stripes are caused by aberrations at large resonant scan angles.

643

644 **Figure 4. Point spread functions.**

645 Point spread functions were measured at 13 different positions in the field at the middle
646 depth of the imaging volume. The sample consisted of fluorescent microbeads (diameter,
647 0.5 μ m, embedded in 1 mm thick 1.5% agar, under 450 μ m of coverglass) imaged at
648 970 nm. The excitation intensity was 8.75 mW, below excitation saturation of the beads.
649 At each position, a 61 μ m x 61 μ m x 35 μ m volume (average of 30 acquisitions) was
650 acquired with 8.4 x 8.4 x 2 pixels per μ m. Bead that were separated by at least 2 μ m x 2
651 μ m x 12 μ m from the edges of the volume and other beads were analyzed. 2-13 PSFs per
652 volume were measured.

653 A) Example measurement at the center of the FOV.

654 B) Mean intensity projections through the XY, XZ, and YZ slices of the bead.

655 C) Gaussian fit through the lateral slice through the bead image.

656 D) Same as C), axial slice.

657 E-H) Same as A-D) for a bead at the edge of the FOV (2.4 mm from the center on the
658 top).

659 I) Average lateral full-width-at-half-max (FWHM) of the central XY slice of a
660 bead, averaged across the X and Y directions.

661 J) Average axial FWHM.

662 K) Average normalized brightness of the beads. Error bars, standard deviation.

663

664 **Figure 4 Supplement 1. Point spread functions across imaging depth**

665 Point spread functions were measured at five different depths at the center of the FOV.

666 Same sample and imaging conditions as Figure 4.

667 A) Example measurement at the center of the FOV close to the cover glass at the top of
668 the sample.

669 B) Mean intensity projections through the XY, XZ, and YZ slices of the bead.

670 C) Gaussian fit through the lateral slice through the bead image.

671 D) Same as C), axial slice.

672 E-H) Same as A-D) for a bead at the bottom of the imaging volume (RF set to 1 mm
673 deep).

674 I) Average lateral full-width-at-half-max (FWHM) of the central XY slice of a bead,
675 averaged across the X and Y directions.

676 J) Average axial FWHM.

677 K) Average normalized brightness of the beads. Error bars, standard deviation.

678

679 **Figure 4 Supplement 2. Point spread functions across the imaging volume**

680 Point spread functions were measured at 15 different locations across the imaging
681 volume. Three planes (depths; 0 μm , blue; 300 μm , grey; 800 μm , red) were sampled
682 using the RF system. In each plane, five regions of the FOV were sampled, including the
683 center and four extrema (2.4 mm from the center) in all quadrants (see legend). Same
684 sample and imaging conditions as Figure 4.

685 A) Average lateral full-width-at-half-max (FWHM) of the central XY slice of a bead,
686 averaged across the X and Y directions.

687 B) Average axial FWHM.

688 C) Average normalized brightness of the beads. Error bars, standard deviation.

689

690 **Figure 4 Supplement 3. Point spread functions at different excitation wavelengths.**

691 Point spread functions were measured at the center of the FOV for different excitation
692 wavelengths. For each wavelength dispersion compensation was adjusted to give
693 maximum signal from a fluorescein bath and same average power was used (conditions
694 otherwise as in Figure 4).

695 A) Average lateral full-width-at-half-max (FWHM).

696 B) Average axial FWHM.

697

698 **Figure 4 Supplement 4. Point spread functions as a function of coverglass angle**

699 A) Schematic illustrating how PSF size was measured at different coverglass angles.

700 B) Mean intensity projections through the XZ slices of a bead at different coverglass
701 angles.

702 C) Average lateral full-width-at-half-max (FWHM) .

703 D) Average axial FWHM.

704

705 **Figure 5. Measurement of collection efficiency.**

706 A) Apparatus for measuring signal collection across the FOV and determining the NA of
707 the collection optics. The light source consisted of a LED (530 nm) and adjacent pinhole,
708 with a miniature optical relay that projected the pinhole onto the top of a microscope
709 slide. The projected spot had a 460 μm diameter. An aperture in the relay could be
710 adjusted to change the NA of the light source from 0 to 1.

711 B) Normalized signal intensity measured with the PMT (not shown in A) as a function of
712 position of the light source. The objective was moved in a 0.5 mm grid relative to the
713 light source. Right, Y slice through the center of the image. Left, X slice through the
714 center of the image. The peak signal was located off the main two axes.

715 C) Signal intensity measured by the PMT as a function of the numerical aperture of the
716 light source (blue) overlaid on the power entering the objective (gray). As the NA of the
717 light source increases the power entering the objective scales approximately as the square
718 of the NA, as expected. The power entering the objective was measured with a high NA

719 accepting power meter (Thor; S170C). Measurement was taken with the 460 μm spot in
720 the center of the field.

721 D) Peak normalized ratio of the intensity measured by the PMT to the power entering the
722 objective as a function of the NA of the light source (axis sampled non-uniformly). The
723 signal intensity measured through the collection optics scales with the power entering the
724 objective until it drops off around NA 1.0, significantly larger than the 0.6 excitation NA
725 of the objective.

726

727 **Figure 6. Characterization and correction of field curvature**

728 A) Field curvature was measured using a thin fluorescein sample (11.2 μm , sandwiched
729 between a microscope slide and 450 μm of coverglass, imaging conditions as in Figure
730 3A). At a particular RF position the image of the sample was a fluorescent ring. We
731 measured the diameter of the ring as a function of RF position.

732 B) Image of the sample without any correction for field curvature. The sample appears as
733 a thin ring.

734 C) Measured field curvature (gray: before field curvature correction, blue: after field
735 curvature correction).

736 D) The RF mirror was programmed to compensate for the field curvature. The
737 compensation is done on a line-by-line basis using the average position of the resonant
738 mirror during the line as the point to correct. This compensation is able to correct the
739 field curvature along each stripe well (top), but is unable to correct the field curvature
740 within a resonant scan as the resonant mirror moves too fast (bottom).

741

742 **Figure 6 Supplement 1. Characterization of remote focus mirror positioner (voice 743 coil).**

744 A) Motion profile (blue) during of the RF mirror during a 300 μm move of the focal
745 position. The command signal (grey) contained a 3.3 ms ramp to prevent oscillations of
746 the actuator. Inset corresponds to a zoom during the settle period.

747 B) The step and settle times (to $< 2.5 \mu\text{m}$) as a function of step size.

748

749 **Figure 7. Imaging fluorescent proteins in anesthetized transgenic mice**

750 A) Low magnification image (one section, 120 μm below the dura). The mouse expressed
751 GCaMP6f under the thy-1 promoter (GP 5.17 line). Scanning parameters as in Fig. 1Di.
752 Field curvature correction was enabled. Average of 30 scans; power 120 mW.

753 B) Higher magnification image (dashed box in A). Scanning parameters as in Fig. 1Dii.

754 C) Low magnification image (one section, 200 μm below the dura). The mouse expressed
755 GCaMP6s under the thy-1 promoter (GP 4.3 line). Scanning parameters as in Fig. 1Di.
756 Field curvature correction was enabled. Average of 30 scans; power 120 mW. Data
757 corresponds to Movie 1.

758 D) Higher magnification image (dashed box in C). Single neurons with nuclear excluded
759 GCaMP are clearly visible.

760 E) Low magnification image at a deeper focal plane (one section, 450 μm below the
761 dura). Same mouse and scanning parameters as C); power 175 mW.

762 F) Higher magnification image (dashed box in E) showing major somatosensory areas in
763 layer 4. These areas appear as regions with reduced fluorescence since GCaMP6s
764 expression is minimal in layer 4 stellate cells.

765

766 **Figure 7 Supplement 1. Overlay of a typical field of view with the reference atlas.**

767 A) Overlay of the image from Figure 7E with the mouse cortex (from Allen Brain Atlas,
768 Brain Explorer 2). MOp: primary somatomotor, MOs: secondary somatomotor, SSp-ul:
769 primary somatosensory upper limb, SSp-ll: primary somatosensory lower limb, SSp-un:
770 primary somatosensory unassigned, SSp-tr: primary somatosensory trunk, SSp-bfd:
771 primary somatosensory barrel field, PTLp: posterior parietal association, RSP:
772 retrosplenial, VISam: anteromedial visual, VISpm: posteromedial visual, VISp: primary
773 visual.

774

775 **Figure 7 Supplement 2. Counting nuclei**

776 A) Max projection, 100 μm to 200 μm deep, imaged in a mouse expressing GFP in the
777 nuclei of excitatory neurons (emx1-cre x Isl-h2b-GFP). The image was locally contrast
778 enhanced with a contrast-limited adaptive histogram equalization (CLAHE, scikit-
779 image).

780 B) Blow-up of a single section showing automatically detected nuclei in red. Nuclei were
781 detected in 3D using a local peak finding algorithm (peak_local_max, scikit-image) after
782 median filtering.

783 C) Number of detected nuclei per 2 μm thick slice, smoothed with a length 3 median
784 filter.

785

786 **Figure 7 Supplement 3. Dendritic images**

787 A) One slice through a mouse expressing YFP in a subset of neurons.

788 B) Zoom in over a dendrite with clearly visible spines.

789

790 **Figure 8. *In vivo* imaging of neural activity**

791 A) Low magnification image from a mouse expressing GCaMP6f under the thy-1
792 promoter (GP 5.17 line) (parameters described in Figure 1Div; 120 mW average laser
793 power). Sampling rate, 4.3 Hz.

794 B) Cross-correlation map of the mean activity in region 1 with the activity in all pixels
795 after smoothing with a 5x5 pixel boxcar filter. A highly correlated spot of activity is
796 visible around region 1.

797 C) Four fields of view (corresponding to boxes in A) that were acquired at high
798 resolution and frame rate (scan parameters describe in Figure 1Dv; power, 120 mW;
799 sampling rate, 9.6 Hz). Regions of interest (orange) were manually drawn around
800 individual neurons.

801 D) Each neuron from the four fields of view colored according to its correlation value
802 with the average activity in region 1. The average activity in region 1 was computed by
803 taking the maximum values across all the $\Delta F/F$ traces in that region.

804 E) $\Delta F/F$ traces for 16 neurons extracted from the four separate regions (four per
805 region) colored according to their correlation coefficient shown in D. Sampling rate,
806 9.6 Hz. Data corresponds to Movie 3.

807 F) Histograms of the correlation coefficients for the neurons in D in the four separate
808 regions.

809

810 **Figure 8 Supplement 1. Neural activity in a large field of view**

- 811 A) Image from a mouse expressing GCaMP6s under the thy-1 promoter (GP 4.3 line)
812 (parameters described in Figure 1Diii, FOV 4.4 mm x 4.2 mm; 120 mW average laser
813 power; sampling rate 1.9 Hz). Image corresponds to Movie 3.
814 B) Local correlation image, showing the result of cross-correlating each pixel with a 4-
815 pixel neighborhood around it.
816 C) 3179 regions of interest were manually drawn around active neurons, using the local
817 correlation image as a reference.
818 D) $\Delta F/F$ traces for 100 neurons. The neurons were selected based on having high
819 skewness during that time period.

820

821 **Movie 1. Multi-resolution information in a 2p-RAM image stack.**

822 Same data as in Figure 7C.

823

824 **Movie 2. Functional imaging of a large field of view.**

825 Same data as in Figure 8, Supplement 1. Movie data was smoothed and downsampled by
826 a factor of two in time.

827

828 **Movie 3. Low resolution imaging at low speed, followed by multi-area imaging at
829 higher speeds.**

830 Same data as in Figure 8A, C. Low resolution movie data smoothed and downsampled by
831 a factor of three in time. High resolution movie data median filtered in space with filter
832 size two, and smoothed and down sampled by a factor of five in time.

833

834 **Author contributions**

835 **Funding**

836 Howard Hughes Medical Institute (HHMI)

837 NJS, DF, KS

838

839 **Author contributions**

840 NJS, Conception and design, experiments, analysis and interpretation of data, drafting the

841 article; DF, Conception and design, optical and mechanical engineering, experiments,

842 analysis and interpretation of data, revising the article; JK, Conception and design,

843 software development, revising the article; KS, Conception and design, experiments,

844 analysis and interpretation of data, drafting the article.

845

846 **Acknowledgements**

847 We thank Courtney Davis and Simon Peron for help with cranial window surgeries;

848 David Tracy and Julie Bentley for help with optical design; Jon Arnold for mechanical

849 engineering support; Jay Kumler, Dan Sykora, and Matt Falanga (Jenoptik) for help with

850 optical design and testing; Jeff Brooker and Shane Patton (Thorlabs) for custom

851 mechanical engineering; Aaron Kerlin and Vasily Goncharov for help with the remote

852 focus system; Jeremy Freeman for help with analysis; Kaspar Podgorski, Arseny

853 Finkelstein, Na Ji, Simon Peron, and Aaron Kerlin for comments on the manuscript.

854 Code, data, and CAD models at <https://github.com/sofroniewn/2pRAM-paper>.

855

856

857

References

858

859 Ahrens, M. B., M. B. Orger, D. N. Robson, J. M. Li and P. J. Keller (2013). "Whole-brain
860 functional imaging at cellular resolution using light-sheet microscopy." Nature
861 Methods **10**(5): 413-420.

862 Akerboom, J., N. Carreras Calderon, L. Tian, S. Wabnig, M. Prigge, J. Tolo, A. Gordus,
863 M. B. Orger, K. E. Severi, J. J. Macklin, R. Patel, S. R. Pulver, T. J. Wardill, E. Fischer, C.
864 Schuler, T. W. Chen, K. S. Sarkisyan, J. S. Marvin, C. I. Bargmann, D. S. Kim, S. Kugler,
865 L. Lagnado, P. Hegemann, A. Gottschalk, E. R. Schreiter and L. L. Looger (2013).

866 "Genetically encoded calcium indicators for multi-color neural activity imaging and
867 combination with optogenetics." Frontiers in molecular neuroscience **6**: 2.

868 Akerboom, J., T. W. Chen, T. J. Wardill, L. Tian, J. S. Marvin, S. Mutlu, N. C. Calderon, F.
869 Esposti, B. G. Borghuis, X. R. Sun, A. Gordus, M. B. Orger, R. Portugues, F. Engert, J. J.
870 Macklin, A. Filosa, A. Aggarwal, R. A. Kerr, R. Takagi, S. Kracun, E. Shigetomi, B. S.

871 Khakh, H. Baier, L. Lagnado, S. S. Wang, C. I. Bargmann, B. E. Kimmel, V. Jayaraman,
872 K. Svoboda, D. S. Kim, E. R. Schreiter and L. L. Looger (2012). "Optimization of a

873 GCaMP Calcium Indicator for Neural Activity Imaging." The Journal of neuroscience :
874 the official journal of the Society for Neuroscience **32**(40): 13819-13840.

875 Akturk, S., X. Gu, M. Kimmel and R. Trebino (2006). "Extremely simple single-prism
876 ultrashort- pulse compressor." Optics express **14**(21): 10101-10108.

877 Born, M. and E. Wolf (1980). Principles of Optics. Oxford, Pergamon.

878 Botcherby, E. J., C. W. Smith, M. M. Kohl, D. Debarre, M. J. Booth, R. Juskaitis, O.

879 Paulsen and T. Wilson (2012). "Aberration-free three-dimensional multiphoton
880 imaging of neuronal activity at kHz rates." Proc Natl Acad Sci U S A **109**(8): 2919-

881 2924.

882 Chen, T. W., T. J. Wardill, Y. Sun, S. R. Pulver, S. L. Renninger, A. Baohan, E. R.

883 Schreiter, R. A. Kerr, M. B. Orger, V. Jayaraman, L. L. Looger, K. Svoboda and D. S. Kim
884 (2013). "Ultrasensitive fluorescent proteins for imaging neuronal activity." Nature

885 **499**(7458): 295-300.

886 Churchland, M. M., B. M. Yu, M. Sahani and K. V. Shenoy (2007). "Techniques for
887 extracting single-trial activity patterns from large-scale neural recordings." Curr
888 Opin Neurobiol **17**(5): 609-618.

889 Dana, H., T.-W. Chen, A. Hu, B. C. Shields, C. Guo, L. Looger, D. Kim and K. Svoboda
890 (2014). "Thy1-GCaMP6 Transgenic Mice for Neuronal Population Imaging In Vivo."

891 PLoS One **9**(9): e108697.

892 Dana, H., B. Mohar, Y. Sun, S. Narayan, A. Gordus, J. P. Hasseman, G. Tsegaye, G. T.

893 Holt, A. Hu, D. Walpita, R. Patel, J. J. Macklin, C. I. Bargmann, M. B. Ahrens, E. R.

894 Schreiter, V. Jayaraman, L. L. Looger, K. Svoboda and D. S. Kim (2016). "Sensitive red
895 protein calcium indicators for imaging neural activity." eLife **5**.

896 Denk, W., K. R. Delaney, A. Gelperin, D. Kleinfeld, B. W. Strowbridge, D. W. Tank and
897 R. Yuste (1994). "Anatomical and functional imaging of neurons using 2-photon

898 laser scanning microscopy." J. Neurosci. Meth. **54**: 151-162.

899 Denk, W., D. W. Piston and W. W. Webb (1995). Two-photon molecular excitation in
900 laser-scanning microscopy. Handbook of Biological Confocal Microscopy. J. B.
901 Pawley. New York, Plenum Press: 445-458.
902 Denk, W. and K. Svoboda (1997). "Photon upmanship: why multiphoton imaging is
903 more than a gimmick." Neuron **18**: 351-357.
904 Duemani Reddy, G., K. Kelleher, R. Fink and P. Saggau (2008). "Three-dimensional
905 random access multiphoton microscopy for functional imaging of neuronal activity."
906 Nat Neurosci **11**(6): 713-720.
907 Estrada-Silva, F. C., J. Garduno-Mejia, M. Rosete-Aguilar, C. J. Roman-Moreno and R.
908 Ortega-Martinez (2009). "Aberration effects on femtosecond pulses generated by
909 nonideal achromatic doublets." Appl Opt **48**(24): 4723-4734.
910 Fan, G. Y., H. Fujisaki, A. Miyawaki, R. K. Tsay, R. Y. Tsien and M. H. Ellisman (1999).
911 "Video-rate scanning two-photon excitation fluorescence microscopy and ratio
912 imaging with cameleons." Biophysical journal **76**(5): 2412-2420.
913 Feng, G., R. H. Mellor, M. Bernstein, C. Keller-Peck, Q. T. Nguyen, M. Wallace, J. M.
914 Nerbonne, J. W. Lichtman and J. R. Sanes (2000). "Imaging neuronal subsets in
915 transgenic mice expressing multiple spectral variants of GFP." Neuron **28**(1): 41-51.
916 Fu, Y., J. M. Tucciarone, J. S. Espinosa, N. Sheng, D. P. Darcy, R. A. Nicoll, Z. J. Huang
917 and M. P. Stryker (2014). "A cortical circuit for gain control by behavioral state." Cell
918 **156**(6): 1139-1152.
919 Gobel, W., B. M. Kampa and F. Helmchen (2007). "Imaging cellular network
920 dynamics in three dimensions using fast 3D laser scanning." Nat Methods **4**(1): 73-
921 79.
922 Grewe, B. F., F. F. Voigt, M. van 't Hoff and F. Helmchen (2011). "Fast two-layer two-
923 photon imaging of neuronal cell populations using an electrically tunable lens."
924 Biomed Opt Express **2**(7): 2035-2046.
925 Grienberger, C. and A. Konnerth (2012). "Imaging calcium in neurons." Neuron
926 **73**(5): 862-885.
927 Guo, Z. V., N. Li, D. Huber, E. Ophir, D. A. Gutnisky, J. T. Ting, G. Feng and K. Svoboda
928 (2014). "Flow of cortical activity underlying a tactile decision in mice." Neuron
929 **81**(1): 179-194.
930 Harvey, C. D., P. Coen and D. W. Tank (2012). "Choice-specific sequences in parietal
931 cortex during a virtual-navigation decision task." Nature **484**(7392): 62-68.
932 Hernandez, A., V. Nacher, R. Luna, A. Zainos, L. Lemus, M. Alvarez, Y. Vazquez, L.
933 Camarillo and R. Romo (2010). "Decoding a perceptual decision process across
934 cortex." Neuron **66**(2): 300-314.
935 Holekamp, T. F., D. Turaga and T. E. Holy (2008). "Fast three-dimensional
936 fluorescence imaging of activity in neural populations by objective-coupled planar
937 illumination microscopy." Neuron **57**(5): 661-672.
938 Holtmaat, A., T. Bonhoeffer, D. K. Chow, J. Chuckowree, V. De Paola, S. B. Hofer, M.
939 Hubener, T. Keck, G. Knott, W. C. Lee, R. Mostany, T. D. Mrsic-Flogel, E. Nedivi, C.
940 Portera-Cailliau, K. Svoboda, J. T. Trachtenberg and L. Wilbrecht (2009). "Long-term,
941 high-resolution imaging in the mouse neocortex through a chronic cranial window."
942 Nat Protoc **4**(8): 1128-1144.
943 Horikawa, K., Y. Yamada, T. Matsuda, K. Kobayashi, M. Hashimoto, T. Matsu-ura, A.
944 Miyawaki, T. Michikawa, K. Mikoshiba and T. Nagai (2010). "Spontaneous network

945 activity visualized by ultrasensitive Ca(2+) indicators, yellow Cameleon-Nano."
946 Nature Methods **7**(9): 729-732.

947 Huber, D., D. A. Gutnisky, S. Peron, D. H. O'Connor, J. S. Wiegert, L. Tian, T. G. Oertner,
948 L. L. Looger and K. Svoboda (2012). "Multiple dynamic representations in the motor
949 cortex during sensorimotor learning." Nature **484**(7395): 473-478.

950 Ji, N., T. R. Sato and E. Betzig (2012). "Characterization and adaptive optical
951 correction of aberrations during in vivo imaging in the mouse cortex." Proceedings
952 of the National Academy of Sciences of the United States of America **109**(1): 22-27.

953 Kerlin, A. M., M. L. Andermann, V. K. Berezovskii and R. C. Reid (2010). "Broadly
954 tuned response properties of diverse inhibitory neuron subtypes in mouse visual
955 cortex." Neuron **67**(5): 858-871.

956 Lecoq, J., J. Savall, D. Vucinic, B. F. Grewe, H. Kim, J. Z. Li, L. J. Kitch and M. J. Schnitzer
957 (2014). "Visualizing mammalian brain area interactions by dual-axis two-photon
958 calcium imaging." Nature Neuroscience **17**(12): 1825-1829.

959 Madisen, L. and e. al (2015). "Transgenic mice for intersectional targeting of neural
960 sensors and effectors with high specificity
961 and performance." Neuron **85**(5): 942-958.

962 Mainen, Z. F., M. Maletic-Savatic, S. H. Shi, Y. Hayashi, R. Malinow and K. Svoboda
963 (1999). "Two-photon imaging in living brain slices." Methods **18**: 231-239.

964 McConnell, G., J. Tragardh, R. Amor, J. Dempster, E. Reid and W. B. Amos (2016). "The
965 mesolens project at the University of Strathclyde." F1000Res.

966 Nagai, T., S. Yamada, T. Tominaga, M. Ichikawa and A. Miyawaki (2004). "Expanded
967 dynamic range of fluorescent indicators for Ca2+ by circularly permuted yellow
968 fluorescent proteins." Proc Natl Acad Sci U S A **101**(29): 10554-10559.

969 Oheim, M., E. Beaurepaire, E. Chaigneau, J. Mertz and S. Charpak (2001). "Two-
970 photon microscopy in brain tissue: parameters influencing the imaging depth." J
971 Neurosci Methods **111**(1): 29-37.

972 Okun, M., N. A. Steinmetz, L. Cossell, M. F. Iacaruso, H. Ko, P. Bartho, T. Moore, S. B.
973 Hofer, T. D. Mrsic-Flogel, M. Carandini and K. D. Harris (2015). "Diverse coupling of
974 neurons to populations in sensory cortex." Nature **521**(7553): 511-515.

975 Peron, S., T. W. Chen and K. Svoboda (2015a). "Comprehensive imaging of cortical
976 networks." Curr Opin Neurobiol **32**: 115-123.

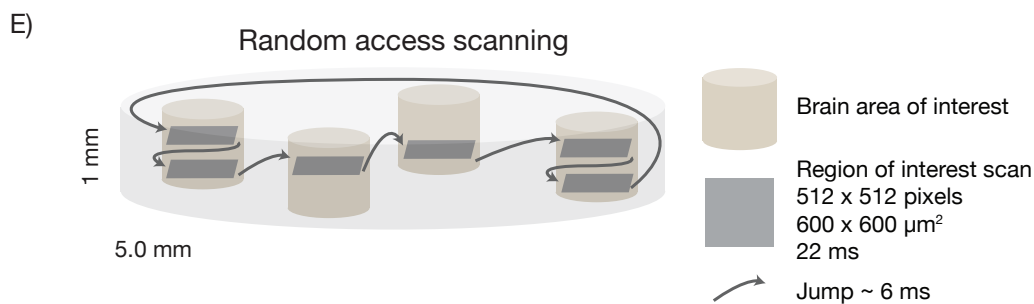
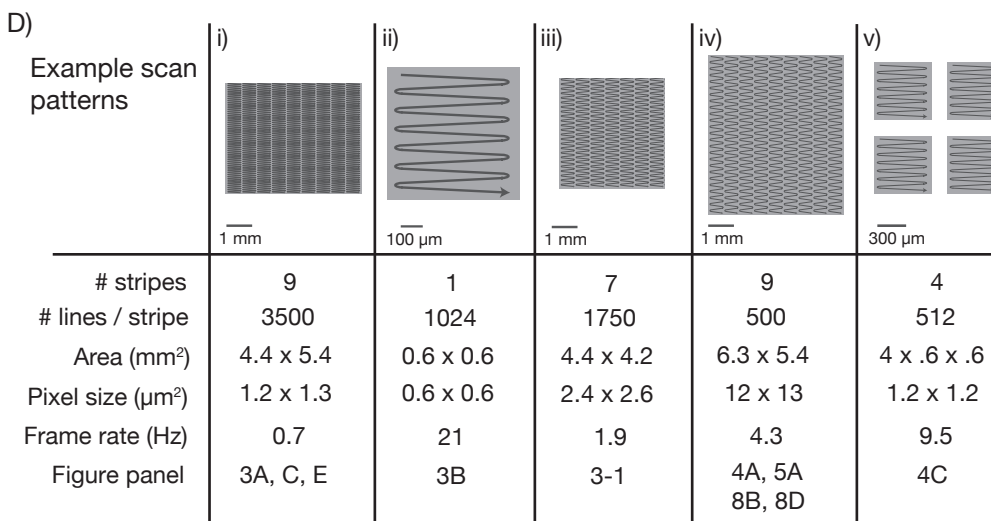
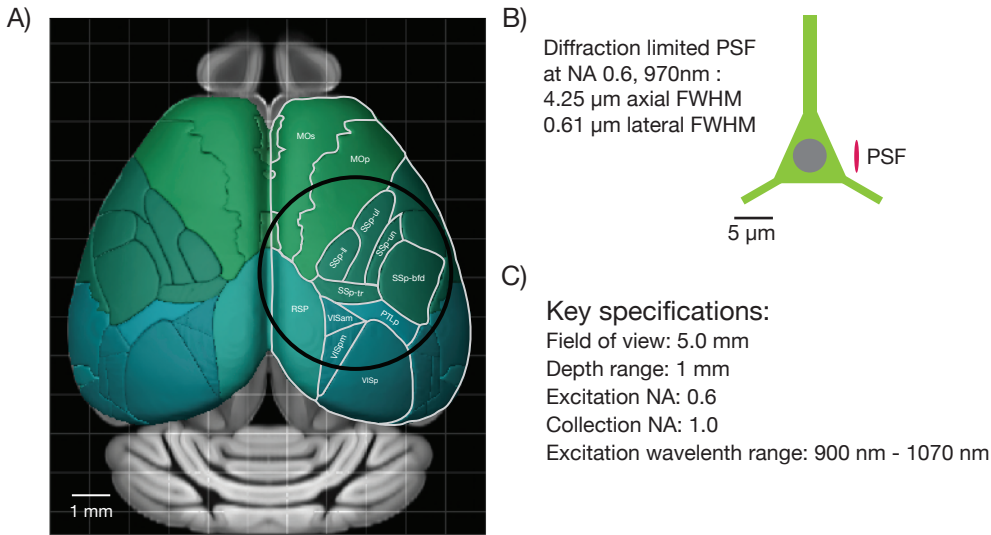
977 Peron, S. P., J. Freeman, V. Iyer, C. Guo and K. Svoboda (2015b). "A Cellular
978 Resolution Map of Barrel Cortex Activity during Tactile Behavior." Neuron **86**(3):
979 783-799.

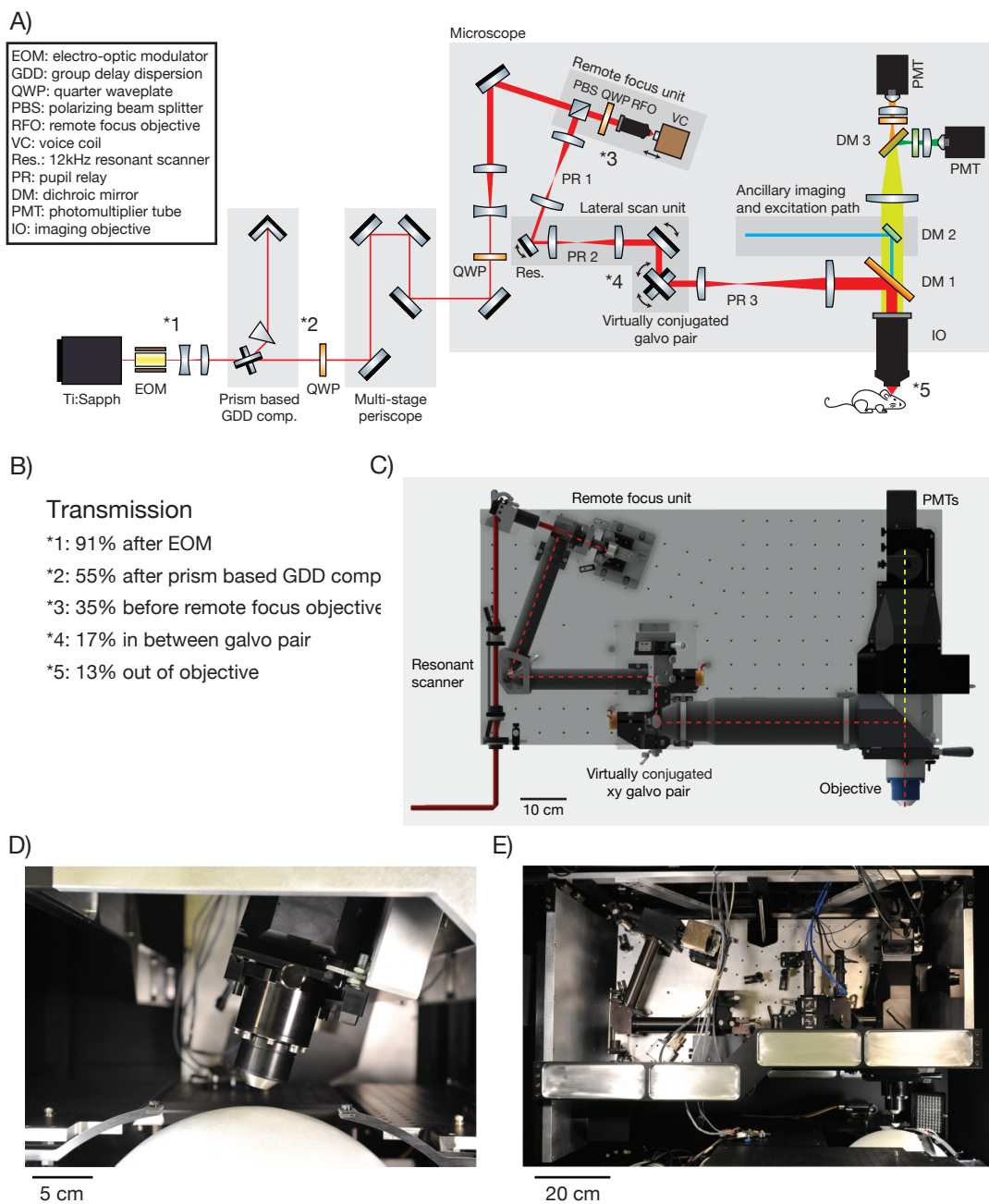
980 Peters, A. and I. R. Kaiserman-Abramof (1970). "The small pyramidal neuron of the
981 rat cerebral cortex. The perikaryon, dendrites and spines." Am J Anat **127**(4): 321-
982 355.

983 Petreanu, L., D. A. Gutnisky, D. Huber, N. L. Xu, D. H. O'Connor, L. Tian, L. Looger and
984 K. Svoboda (2012). "Activity in motor-sensory projections reveals distributed
985 coding in somatosensation." Nature **489**(7415): 299-303.

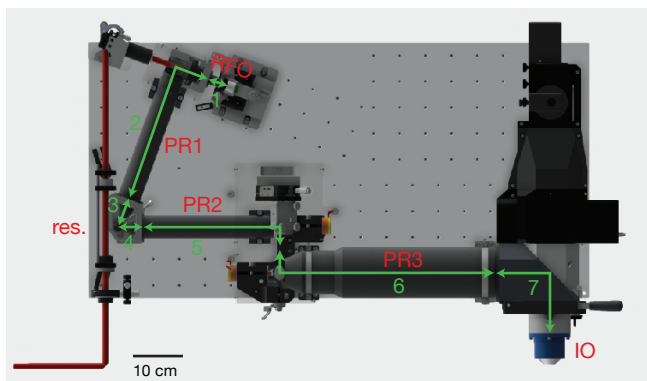
986 Prevedel, R., Y. G. Yoon, M. Hoffmann, N. Pak, G. Wetzstein, S. Kato, T. Schrodell, R.
987 Raskar, M. Zimmer, E. S. Boyden and A. Vaziri (2014). "Simultaneous whole-animal
988 3D imaging of neuronal activity using light-field microscopy." Nature Methods
989 **11**(7): 727-730.

- 990 Reddy, G. D. and P. Saggau (2005). "Fast three-dimensional laser scanning scheme
991 using acousto-optic deflectors." Journal of biomedical optics **10**(6): 64038.
- 992 Sato, T. R., N. W. Gray, Z. F. Mainen and K. Svoboda (2007). "The Functional
993 Microarchitecture of the Mouse Barrel Cortex." PLoS Biol **5**(7): e189.
- 994 Sofroniew, N. J., J. D. Cohen, A. K. Lee and K. Svoboda (2014). "Natural whisker-
995 guided behavior by head-fixed mice in tactile virtual reality." The Journal of
996 neuroscience : the official journal of the Society for Neuroscience **34**(29): 9537-
997 9550.
- 998 Sofroniew, N. J., Y. A. Vlasov, S. Andrew Hires, J. Freeman and K. Svoboda (2015).
999 "Neural coding in barrel cortex during whisker-guided locomotion." eLife **4**.
- 1000 Stirman, J. N., I. T. Smith , M. W. Kudenov and S. L. Smith (2014). "Wide field-of-view,
1001 twin-region two-photon imaging across extended cortical networks." bioRxiv.
- 1002 Stirman, J. N., I. T. Smith , M. W. Kudenov and S. L. Smith (2015). "Wide field-of-view,
1003 twin-region two-photon imaging across extended cortical networks." bioRxiv.
- 1004 Stosiek, C., O. Garaschuk, K. Holthoff and A. Konnerth (2003). "In vivo two-photon
1005 calcium imaging of neuronal networks." Proc Natl Acad Sci U S A **100**(12): 7319-
1006 7324.
- 1007 Tian, L., S. A. Hires, T. Mao, D. Huber, M. E. Chiappe, S. H. Chalasani, L. Petreanu, J.
1008 Akerboom, S. A. McKinney, E. R. Schreiter, C. I. Bargmann, V. Jayaraman, K. Svoboda
1009 and L. L. Looger (2009). "Imaging neural activity in worms, flies and mice with
1010 improved GCaMP calcium indicators." Nat Methods **6**(12): 875-881.
- 1011 Trachtenberg, J. T., B. E. Chen, G. W. Knott, G. Feng, J. R. Sanes, E. Welker and K.
1012 Svoboda (2002). "Long-term in vivo imaging of experience-dependent synaptic
1013 plasticity in adult cortex." Nature **420**(6917): 788-794.
- 1014 Tsai, P. S., C. Mateo, J. J. Field, C. B. Schaffer, M. E. Anderson and D. Kleinfeld (2015).
1015 "Ultra-large field-of-view two-photon microscopy." Optics express **23**(11): 13833-
1016 13847.
- 1017 Tsai, P. S., N. Nishimura, E. J. Yoder, A. White, E. Dolnick and D. Kleinfeld (2002).
1018 Principles, design and construction of a two photon scanning microscope for in vitro
1019 and in vivo studies. Methods for In Vivo Optical Imaging. R. Frostig. Boca Raton, CRC
1020 Press: 113-171.
- 1021 Vanni, M. P. and T. H. Murphy (2014). "Mesoscale transcranial spontaneous activity
1022 mapping in GCaMP3 transgenic mice reveals extensive reciprocal connections
1023 between areas of somatomotor cortex." J Neurosci **34**(48): 15931-15946.
- 1024 Wilt, B. A., J. E. Fitzgerald and M. J. Schnitzer (2013). "Photon shot noise limits on
1025 optical detection of neuronal spikes and estimation of spike timing." Biophysical
1026 journal **104**(1): 51-62.
- 1027 Zhao, Y., S. Araki, J. Wu, T. Teramoto, Y. F. Chang, M. Nakano, A. S. Abdelfattah, M.
1028 Fujiwara, T. Ishihara, T. Nagai and R. E. Campbell (2011). "An expanded palette of
1029 genetically encoded Ca(2) indicators." Science **333**(6051): 1888-1891.
- 1030 Zipfel, W. R., R. M. Williams and W. W. Webb (2003). "Nonlinear magic: multiphoton
1031 microscopy in the biosciences." Nature biotechnology **21**(11): 1369-1377.
- 1032 Ziv, Y., L. D. Burns, E. D. Cocker, E. O. Hamel, K. K. Ghosh, L. J. Kitch, A. El Gamal and
1033 M. J. Schnitzer (2013). "Long-term dynamics of CA1 hippocampal place codes." Nat
1034 Neurosci **16**(3): 264-266.
- 1035



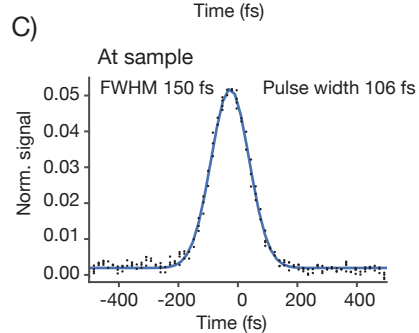
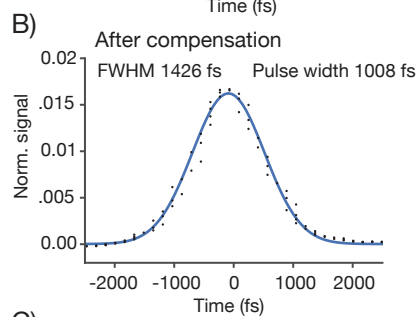
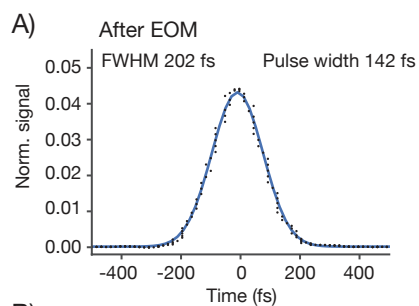


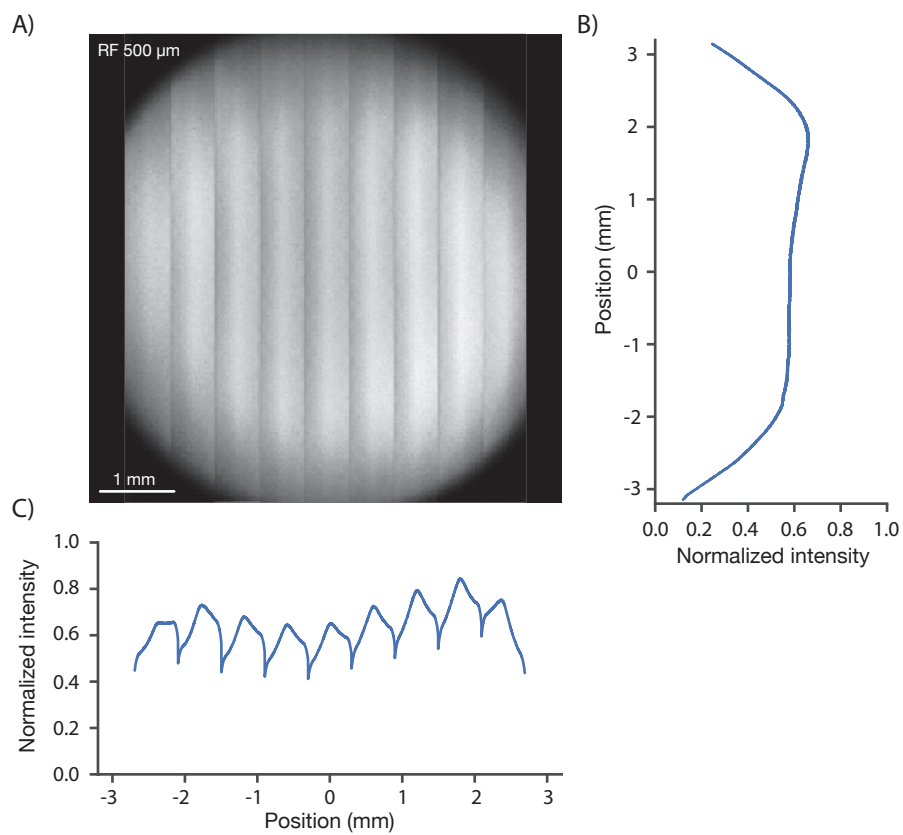
A)

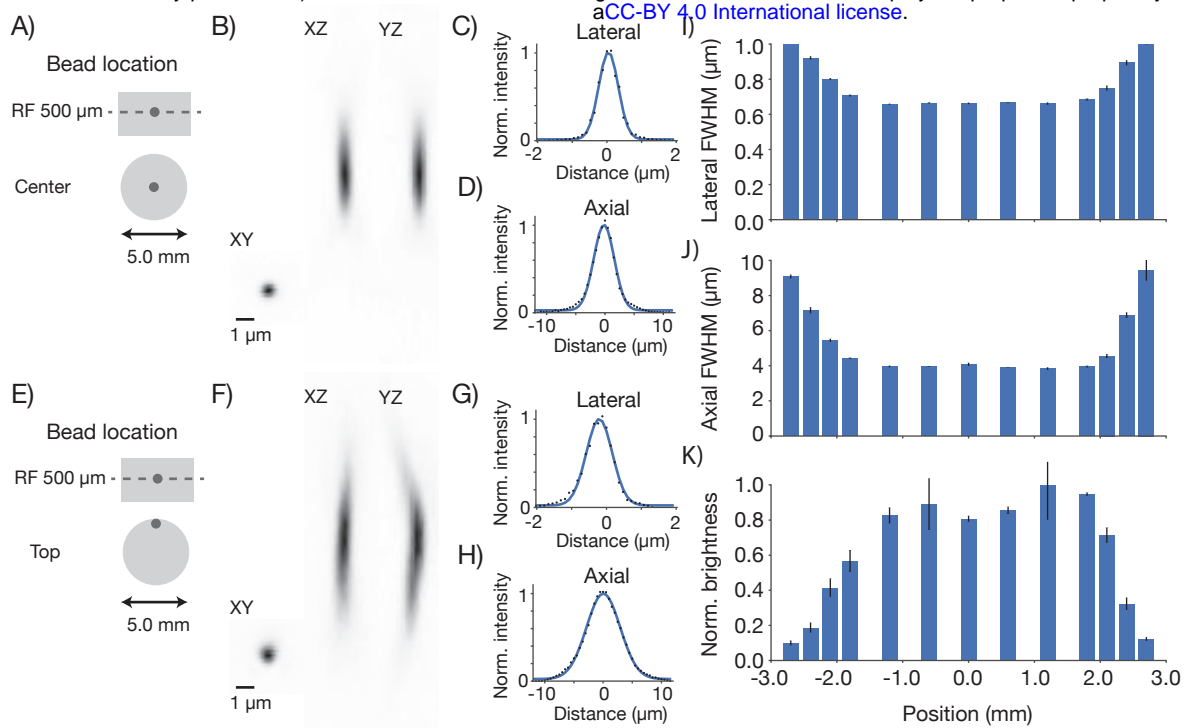


- 1: RFO mounting flange to RF mirror: 32.50 mm
- 2: PR1 mounting flange to RFO mounting flange: 341.43 mm
- 3: PR1 mounting flange to res. mirror: 57.95 mm
- 4: PR2 mounting flange to res. mirror: 46.01 mm
- 5: PR2 mounting flange to single xy point: 399.68 mm
- 6: PR3 inside mounting flange to single xy mirror point: 423.88 mm
- 7: PR3 inside mounting flange to top surface of IO flange: 224.05 mm

Figure 2 Supplement 2







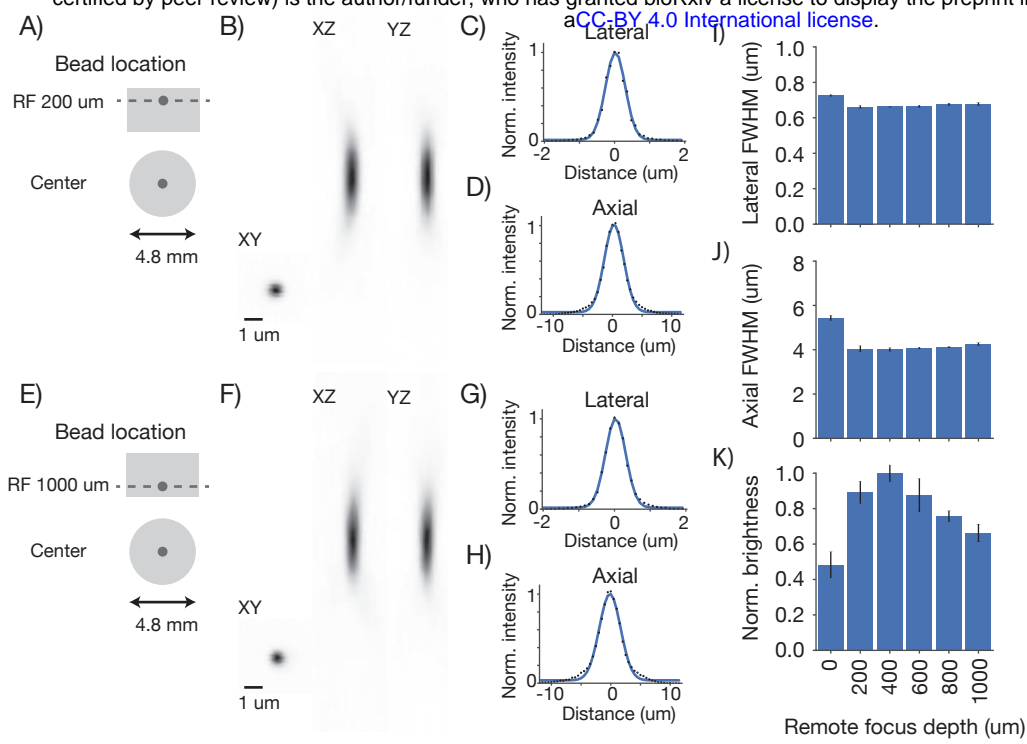


Figure 4
Supplement 1

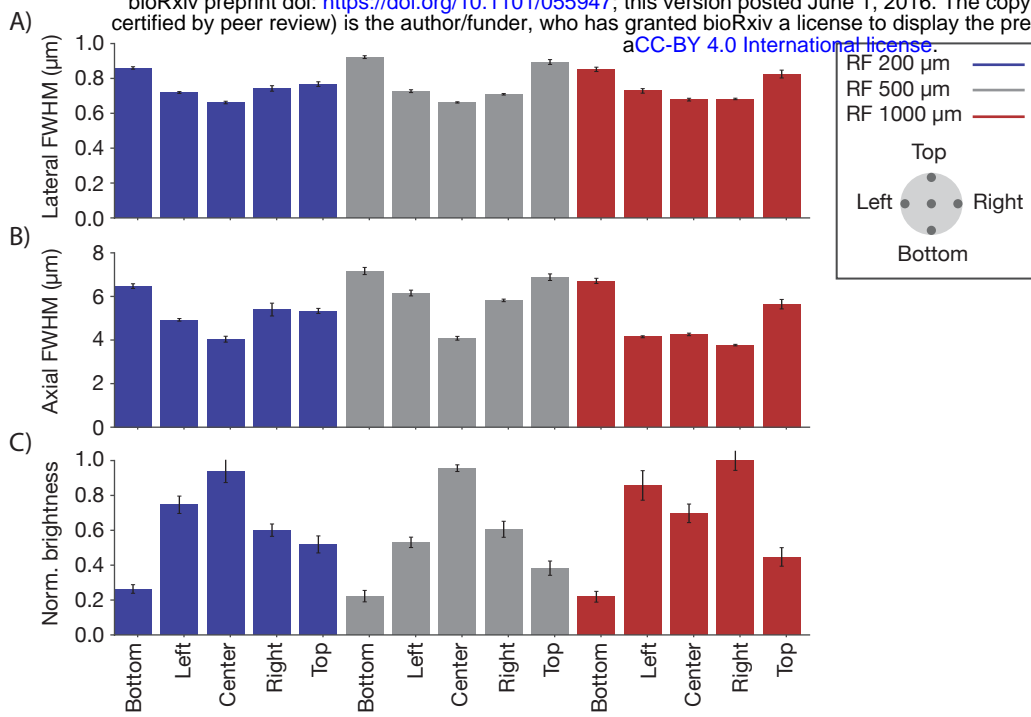
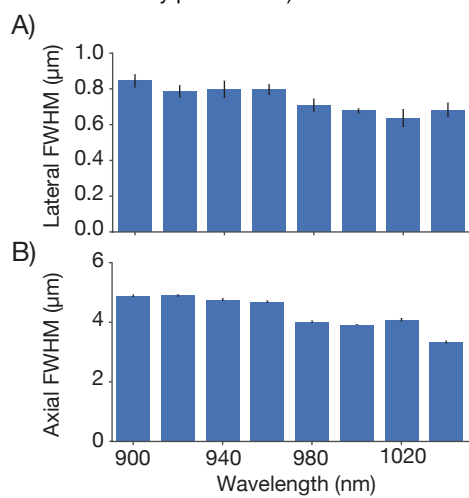


Figure 4
Supplement 2



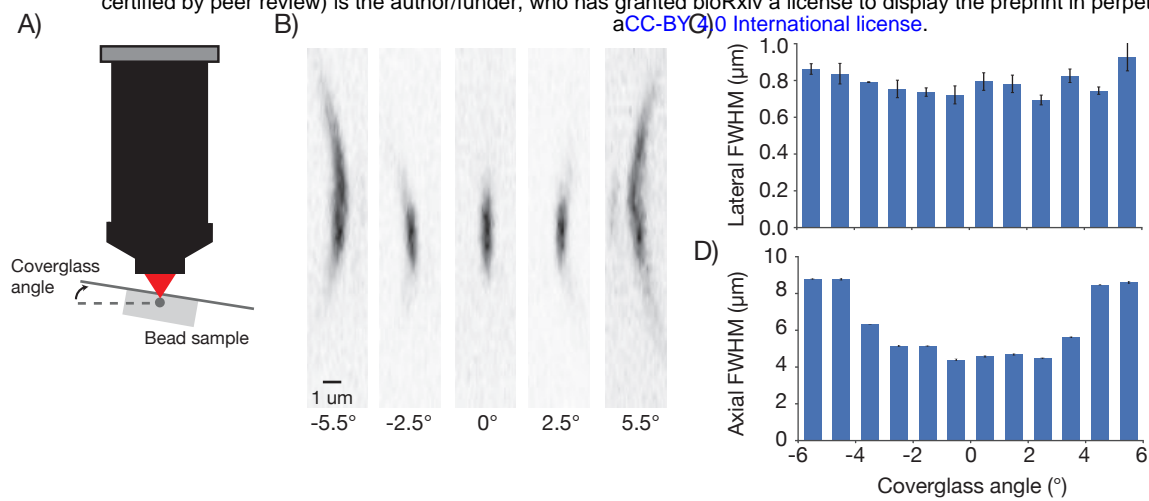
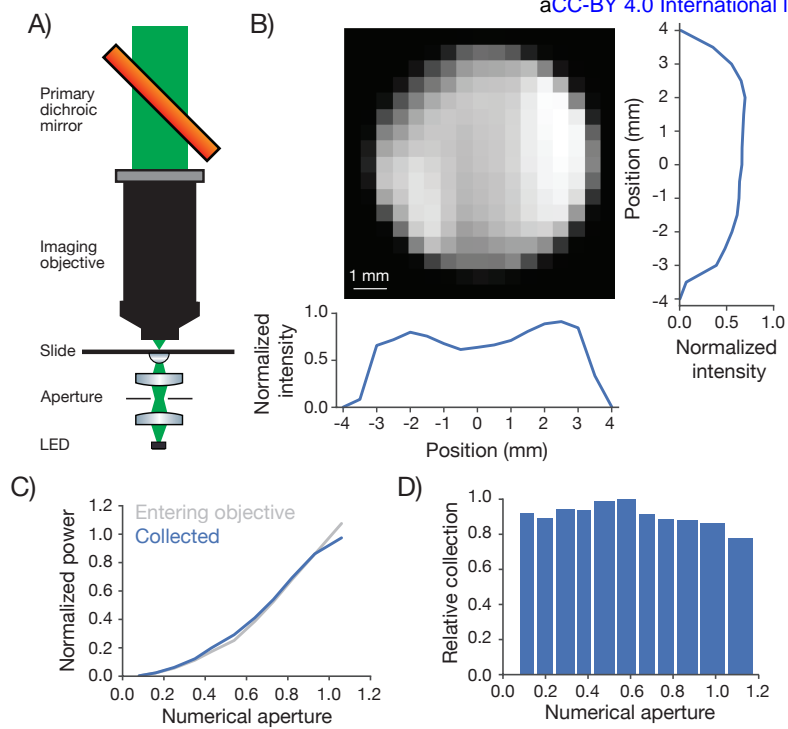
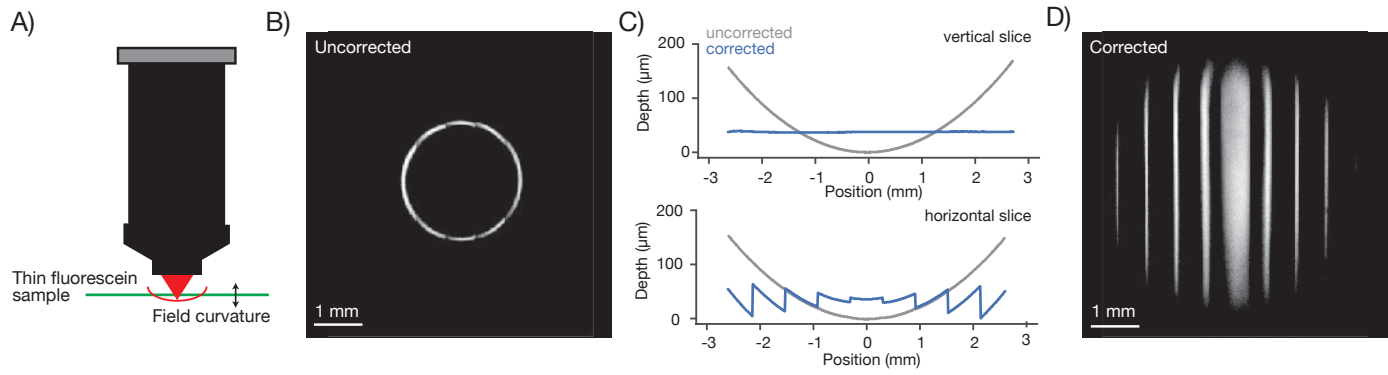
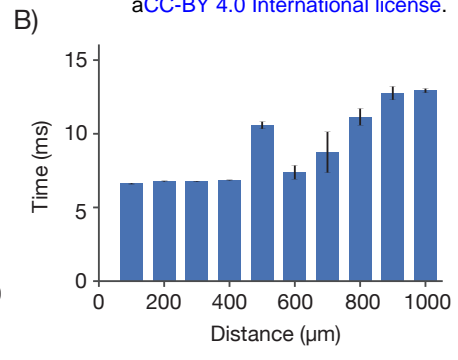
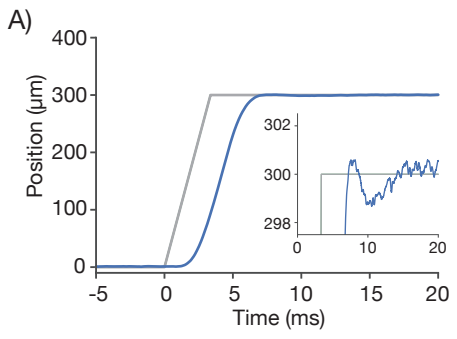


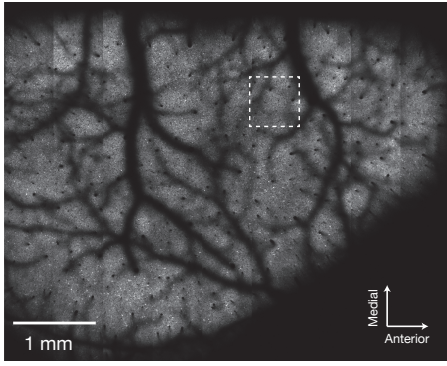
Figure 4
Supplement 4



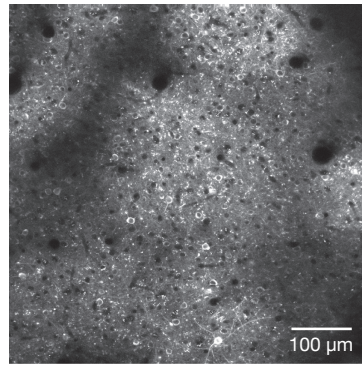




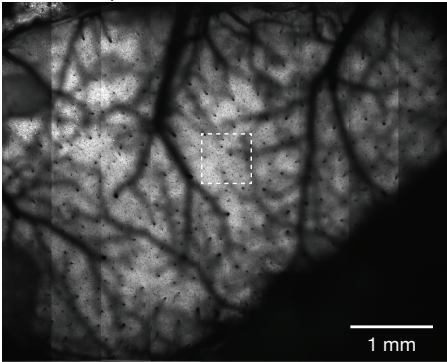
A) 120 μm deep - GP5.17



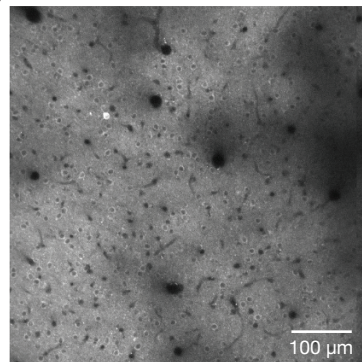
B)



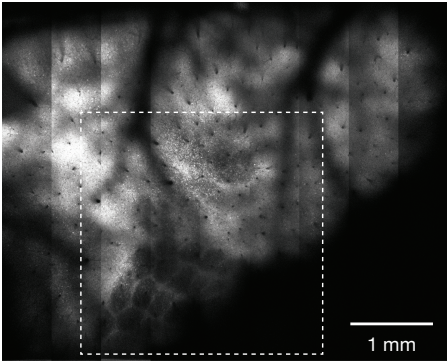
C) 200 μm deep - GP4.3



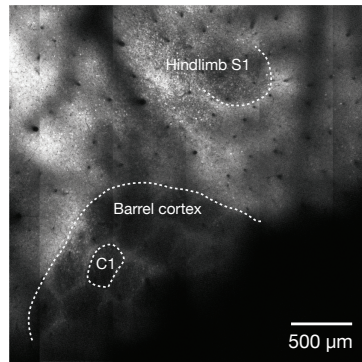
D)



E) 450 μm deep - GP4.3



F)



A)

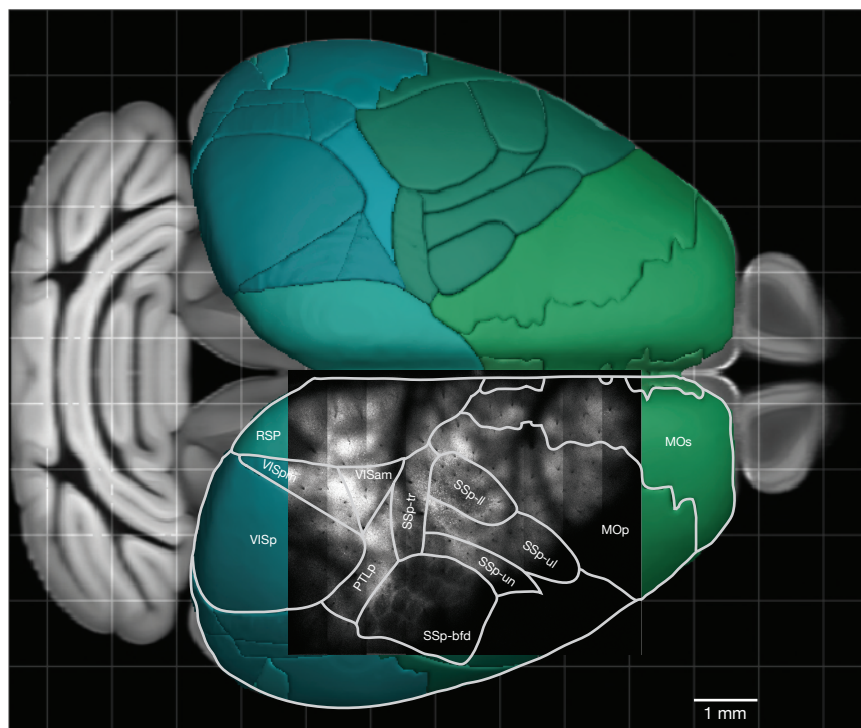
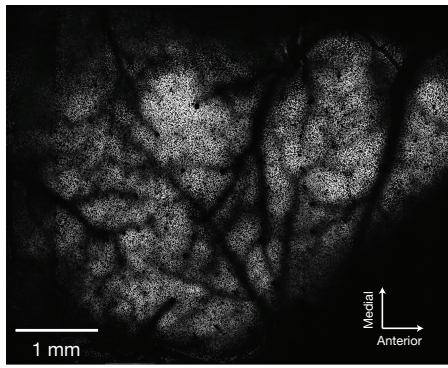
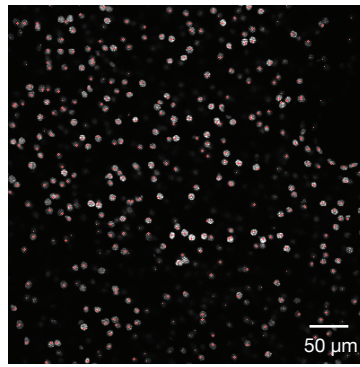


Figure 7
Supplement 1

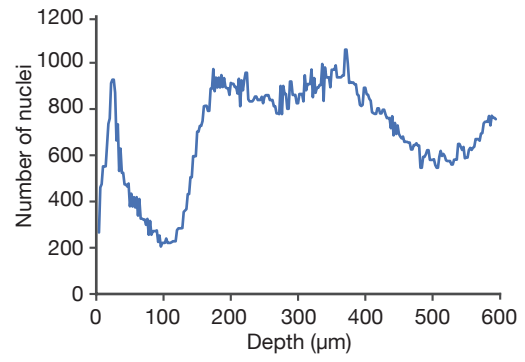
A) *emx1-cre x Isl-1^{2D}-GFP*
100 - 200 μ m max projection



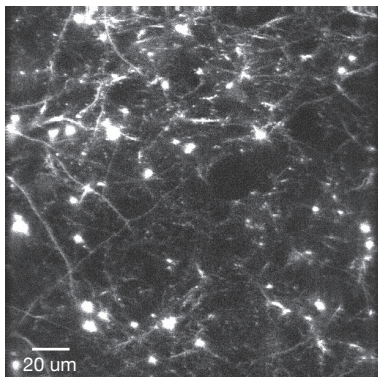
B)



C)



A)



B)

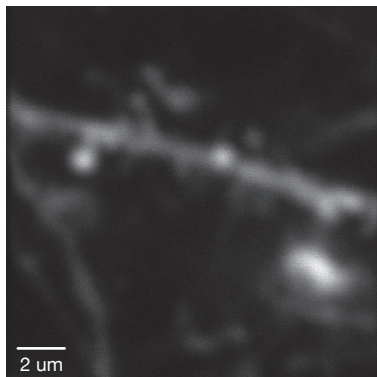


Figure 7
Supplement 3

